Sedimentation and viscosity controls on forearc high growth

David Fernández-Blanco[1], Utsav Mannu[2,3], Teodoro Cassola[4], Giovanni Bertotti[1] & Sean D. Willett[3]

[1]Department of Geoscience and Engineering, Faculty of Civil Engineering and Geosciences, Delft, University of Technology, Stevinweg 1, 2628 CN, Delft, the Netherlands

[2] Department of Earth and Climate Science, IISER Pune, Dr. Homi Bhabha Road, Pashan, Pune, 411008, India

[3] Geological Institute, Swiss Federal Institute of Technology (ETH), 8092 Zürich, Switzerland

[4] Schlumberger GmbH, Ritterstrasse 29, 52072 Aachen, Germany

Abstract

Crustal rheology and surface processes strongly influence strain distribution and shape of orogenic wedges at their front but how they influence the wedge rear is still unclear. Here, we analyze the coupled control of viscosity and sedimentation on forearc high growth during advanced stages of subduction accretion. We use 2D thermo-mechanical finite element models constrained with data of the south Anatolian margin. Our simulations show that forearc highs grow as a thermally-activated viscosity drop in the lower crust induces ductile deformation and viscous flow. Initial viscosity and the amount of sediments in the forearc basin control non-linearly the occurrence and timing of the thermally-activated viscosity drop, and thus of the growth of the forearc high. High sedimentation rates result in thicker forearc basins that stabilize the subduction wedge and delay the onset of uplift in the forearc high. Low viscosities promote earlier onset of forearc high uplift and lead to larger morphological variability along the subduction margin. Increasing either sedimentation rate or viscosity may prevent forearc high formation entirely. Forearc highs grow without a backstop at a location set by slab geometry, and at an age set by wedge thermal state. Our models explain vertical motions in south Anatolia and potentially in other accretionary margins, like the Lesser Antilles or Cascadia, during the formation of their broad forearc highs.

Keywords: orogenic wedge; forearc; forearc basin; outer-arc high; uplift; Turkey; Central Anatolian Plateau

Introduction

Orogenic wedges growing by accretion develop characteristic cross-sectional shapes that result from the balance between basal traction in the subduction thrust and gravity, as modulated by orogenic wedge rheology and internal strain (Davis *et al.*, 1983; Platt, 1986; Willett, 1992). The geometry of the wedge front is controlled by brittle deformation, and prescribed by the mechanical properties of the accreting wedge and that of its surface of accretion (Davis *et al.*, 1983; Dahlen, 1984). The geometry of the wedge rear, however, is less well understood, given its dependence on the non-linear ductile dynamics of the deeper sectors of the wedge (Pavlis & Bruhn, 1983).

Orogen rheology and surface processes markedly influence the first-order evolution of accreting orogenic wedges. Syntectonic erosion (e.g., Koons, 1990; Willett, 1999) and sedimentation (e.g., Willett & Schlunegger, 2010; Fillon *et al.*, 2013; Erdős *et al.*, 2015) affect the distribution of strain and the deformation patterns within the wedge. Higher ductility results in structures otherwise absent, like backward thrusting sequences (Smit *et al.*, 2003). How these factors and their feedback influence the development and evolution of topography in the wedge internal sectors is difficult to generalize and often overlooked, limiting our understanding of the dynamic interactions among surface and deep processes at orogenic scale.

Forearc systems in accretionary margins have characteristic trench-parallel structures and derived stratigraphies (Dickinson & Seely, 1979) (Fig. 1). Forearc highs are plateau-like elevated areas developing in internal regions of some, albeit not all, forearc systems, and their formation may be explained by several mechanisms. Forearc highs may form by upward terrain growth during forced mechanical accretion of material against areas with higher relative strength commonly referred to as backstops (e.g., Byrne *et al.*, 1993; Kopp & Kukowski, 2003). Under this viewpoint, the strength contrast controls the formation of the forearc high, its structure and the limits of the wedge (Kopp & Kukowski, 2003).

Alternatively, forearc highs may uplift dynamically, supported by high temperatures and heat production in the deeper sectors of large subduction wedges (e.g., Pavlis & Bruhn, 1983; Vanderhaeghe *et al.*, 2003). In this context, forearc highs may grow by thermal activation of viscosity in the lower crust, guided by sediment deposition in the forearc basin, and ductile deformation sustained by sediment accretion (Fuller *et al.*, 2006a).

In this paper, we focus on this thermo-viscous mechanism of crustal flow and forearc uplift, which has been recently argued to be consistent with the pattern of space-time deformation exhibited by the Cyprus-Anatolia margin (Fernández-Blanco *et al.*, 2020). We elaborate on this model to demonstrate the relationship between sedimentation rates and rheology with temperature, strain patterns and growth of the accretionary wedge. We analyze how syn-accretion sedimentation in the forearc basin and the viscous state of the subduction wedge control the thermo-viscous uplift of the forearc high. We use 2D thermo-mechanical finite element simulations that include critical wedge visco-plastic mechanics and isostatic compensation, as well as variations in sediment input, rheological behavior, and thermal conductivity. We build our models to be consistent with the geometry and geologic history of the Central Cyprus accretionary margin. We perform a parametric study focused on how sedimentation rate and specific viscous rheological parameters influence the temperature distribution, strain rate and localization in the accretionary wedge internal sectors, and specifically under the forearc high area. For all simulations, we focus on the wavelength and relative age of vertical motions in the upper crust. We find that the dynamic growth of forearc highs can take place non-linearly in time and can explain short-wavelength vertical motions in inland sectors of subduction wedges.

2. Forearc elements of accretionary subduction wedges

We define morphotectonic features of arc-trench regions for generic accretionary margins in nature and in simulations and relate them to elements along Central Cyprus (Fig. 1). In

nature, forearcs in accretionary systems exhibit a seaward area under mechanical accretion and an inland area where a forearc basin may be disrupted by a forearc high (Dickinson & Seely, 1979) (Fig. 1A). Imbricate seaward-verging thrusts in the seaward sector increase topography landwards from the trench to the trench-slope break, where landward-verging thrusts result in landward-dipping slopes. A trench-fill basin develops above the trench and accretionary basins lay along the trench-slope region as "piggy-back" basins carried atop thrust sheets. Landward, between the trench-slope break and volcanic arc, the forearc high may divide the forearc basin into residual and intramassif basins (Fig. 1A).

In models, shear zones develop convex-up "structural highs" enclosing convex-down "topographic depressions". We identify both features with respect to the actively deforming sector of the wedge and by location along the model transect (Fig. 1B). In model pro-wedge (seaward), topographic depressions lead to the pro-wedge and wedge-top basins (DeCelles & Giles, 1996). The area of active deformation is limited landward by the structural high, and farther toward the model retro-wedge, the growth of the forearc basin sets a stable area. When present, the forearc structural high defines forearc basins at its front and at its back, named the pro- and retro-wedge forearc basins (Fig. 1B). We use negative-alpha basin both in nature and in models to refer to a basin that has a hypothetical critical slope dipping landward and no internal deformation, as it slides above the subduction thrust for as long as it is restricted and steadily infilled to its bounding highs (Fuller *et al.*, 2006a; Willett & Schlunegger, 2010).

First-order morphotectonic features in the current arc-trench region of Central Cyprus correlate with the elements described above (Fig. 1C). At the southern end of the overriding Anatolian plate, the northern end of the Levantine Basin may be seen as a trench-fill basin. Northward, the Troodos Ophiolite and the piggy-back Mesaoria wedge-top basin compound the trench-slope, and the Kyrenia Range is the trench-slope break. Farther north,

the Cilicia Basin is a residual basin seaward of the Mut Basin, an intramassif basin within the modern Central Taurus forearc high (Fig. 1C).
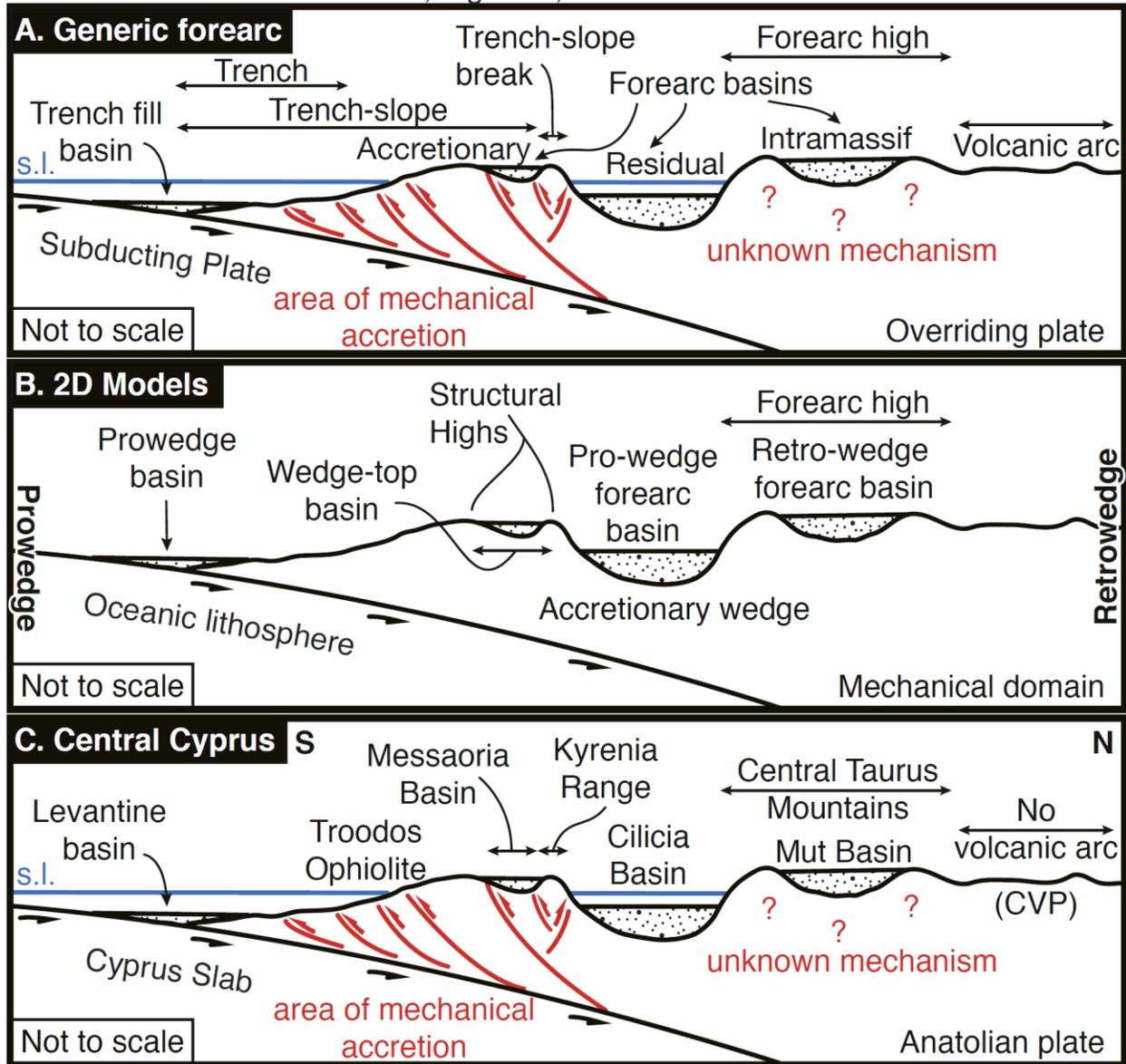

Figure 1. Accretionary margins in nature and models. *Main morphotectonic features in (A) a generic accretionary margin with forearc high, in (B) models of subduction wedge accretion, and (C) their correlation to features in Central Cyprus. For natural examples, we use original definitions by Karig & Sharman (1975) and Dickinson & Seely (1979), and for numerical models a simpler nomenclature (e.g., Fuller, 1996). "Trench-fill basin" and "accretionary forearc basin" are the nature equivalents to "pro-wedge" and "wedge-top" basins in models, and the terms "residual" and "intramassif forearc basins" of Dickinson & Seely (1979) are in simulations the "landward" and "seaward" forearc basins, respectively. Correlation with elements along the Central Cyprus margin is based in Fernández-Blanco et al. (2020).*

Surface uplift of the forearc high of the Central Cyprus subduction margin spans for an area of ~200 km N-S and ~350 km E-W and led to the modern Central Taurus Mountains of South Turkey (Fig. 1). Surface uplift of the modern Central Taurus Mountains occurred since the latest Miocene (post-8Ma) (e.g., Cosentino *et al.*, 2012; Meijers *et al.*, 2018) with no regional fault at the surface (Fernández-Blanco *et al.*, 2019). The underlying causes behind surface uplift in South Turkey remain debated, with several studies proposing slab break-off (see Schildgen *et al.*, 2014 for a review), and more recent work suggesting crustal thickening (Meijers *et al.*, 2018) and ductile flow following thermally-activated viscosity in the lower Anatolian crust (Fernández-Blanco *et al.*, 2020). The latter mechanism is consistent with the thick Anatolian crust and lithosphere and the presence of the Cyprus slab under the modern Central Taurus Mountains (e.g., Bakırcı *et al.*, 2012; Abgarmi *et al.*, 2017; Delph *et al.*, 2017) as well as the coupled, short-wavelength vertical motions reported for South Turkey and its offshore during plateau margin growth (Walsh-Kennedy *et al.*, 2014; Fernández-Blanco *et al.*, 2019).

3. Methods: Thermo-Mechanical Finite Element Models

3.1. Numerical Model Description

We used 2D thermo-mechanical finite element numerical models that simulate a transect whose specific geometry and parameters are selected to fit to the Anatolian margin at the longitude of central Cyprus. Models simulate the thermo-mechanical processes within a deforming forearc, subject to brittle and ductile deformation along with active sedimentation within wedgetop basins. Our models use the numerical formulation described by Fullsack (1995), Pope and Willett (1998), Fuller et al. (2006a, 2006b) and include recent modifications for sedimentation, strain softening and healing, and material tracking (Cassola, 2013).

Our models have two nested and coupled domains (Fig. 2) that solve for mechanical and thermal processes. The mechanical domain represents the crust of an accreting subduction zone and its internal deformation is calculated dynamically as a response to imposed motions at its boundaries. At the base of the mechanical domain, tangential velocities drive accretion of incoming sediments. Imposed tangential velocities are coupled to the overlying crust through a frictional slip boundary condition, permitting complete decoupling depending on tangential and normal stresses. The lower boundary has a discontinuity point, S, that represents the contact between the subducting slab and the continental Moho (Fig. 2). However, the importance of this boundary is reduced by the frictional slip permitted along the slab interface. The thermal domain spans the mechanical domain and the underlying upper mantle, including downgoing slab and upper-plate upper mantle. The velocity and geometry of the slab is specified and thus serves as a kinematic component of the model, used for heat advection, but only as a boundary condition for the mechanical deformation. See more detailed information on the thermal computation in the supplementary material. The slab and the lithosphere of the upper plate are permitted to deform by surface loading on the basis of a flexural isostasy model (Fuller *et al.*, 2006a; Fernández-Blanco *et al.*, 2020). The mechanical model includes a temperature-dependent rheology that sustains brittle/frictional behaviour at low temperatures and a power-law viscous behaviour according to an Arrhenius model relating the tensors of deformation rate, D_{ij}, and stress, σ_{ij}:

$$D_{ij} = A_\mu \sigma_{ij}^{n_\mu} exp\left(\frac{-Q}{RT}\right)$$

(1)

where A_μ and n_μ are constants dependent on the material, Q is the activation energy, R is the molar gas constant, and T is the temperature. Strain resulting from this thermally-activated viscosity is thus neglectable under a certain temperature and is the main constituent of deformation above it. All materials have a brittle, pressure-dependent yield

stress, following a Coulomb criterion. See the supplementary material for more details on model formulation and relevant subroutines, including thermal computation.
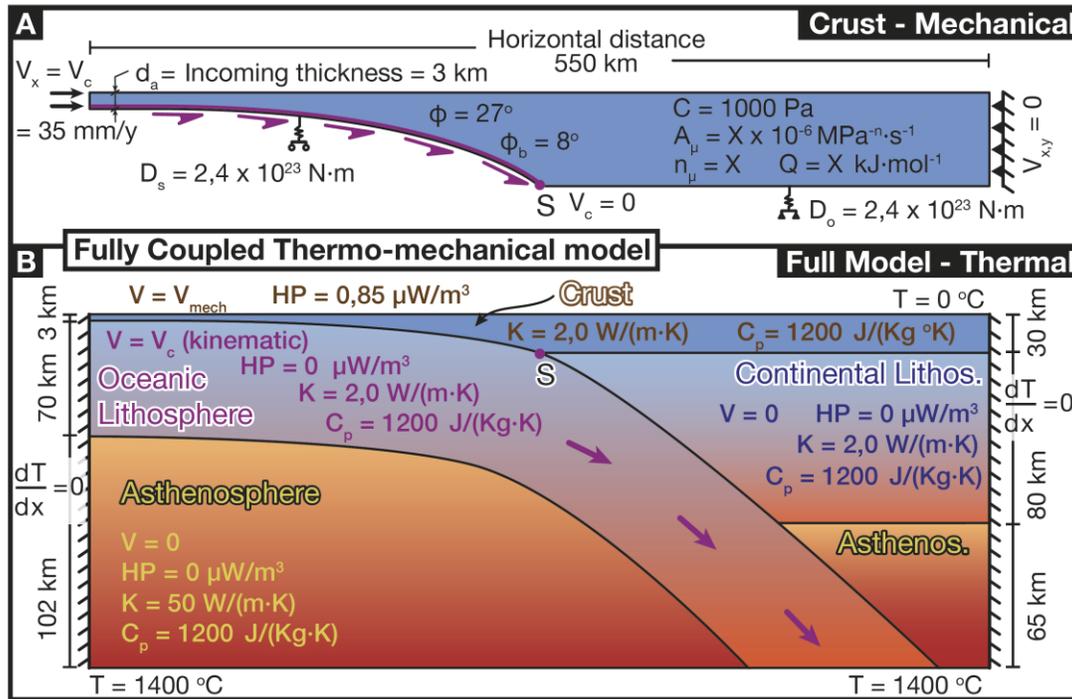

Figure 2. Model setup. *Model setup, with specification of thermal and mechanical parameters. S is the point where the subducting plate contacts the Moho of the upper plate. A set of velocities, V, are defined with regards to a fixed frame in the upper-plate interior: Vx and Vy are the components of velocity in horizontal and vertical directions, respectively, and Vmech is the 2-D velocity in the mechanical domain and is a free variable. Boundary conditions are a constant convergence velocity, Vc, applied to the left side and the base of the subducting plate. Boundary between slab and upper plate has a frictional failure criterion, by which relative slip occurs on boundary once criterion is exceeded. The incoming sediments have a thickness of d_a. D_s is the flexural rigidity of the subducting plate and D_o is that of the overriding plate. The internal friction angle is shown as φ, and the friction angle between plates is φb. Aμ is the coefficient of the power-law viscosity and nμ is its coefficient, with Q being the activation energy. A = heat production, K = thermal conductivity, Cp = specific heat, C = cohesion and T = temperature. Material deforms viscously until yield stress is exceeded, at which point it deforms to satisfy yield criterion.*

3.2 Model design and parameterization

Models simulate 25 My of subduction and accretion along a transect of 550 km (Fig. 2) that corresponds to the Central Cyprus margin (Fernández-Blanco *et al.*, 2020). We use a convergence velocity, Vc = 35 mm/yr, and a thickness of incoming material at the trench of d = 3 km. These two parameters are key to the accretionary flux and thus the growth rate of the accretionary wedge and its final size. Although modern values of these parameters are

higher and lower, respectively, these values are good averages for the timeframe of interest. The present Vc of 9.3 ± 0.3 mm/y in Cyprus (Reilinger *et al.*, 2006) is unrepresentative of the last 25 Ma, given that underthrusting of Eratosthenes Seamount below south Cyprus probably results in a deceleration of the present-day velocity of subduction. Current sedimentary thicknesses between 10 km and 15 km, found in the East Mediterranean (e.g., Makris & Stobbe, 1984), are probably the highest ever present over the entire Neogene, given the increasing sediment supply from the Nile River and the narrowing of the Eastern Mediterranean Sea.

At the model pro-wedge (left side), the subducting lithosphere is 50 My old and has a thickness of 70 km kept constant during the simulations. Since accretion of material from the model pro-wedge thickens the mechanical domain as the models progress, we select an initial thickness of 30 km in the retro-wedge of the mechanical domain which, given our chosen accretionary flux, results in a final thicknesses at the end of model comparable to observed thicknesses (Fig. 3), i.e., maximum values of 45 km near the "S" point. We chose a thickness of 80 km for the rest of the overriding lithosphere.

Flexural rigidity is set at 2.4 x 10^{23} N·m for both plates, but variations of flexural rigidity values of up to four orders of magnitude do not produce substantial changes. The density of the crust is 2.8 g/cc, and is an average value that includes continental and oceanic crusts, and sedimentary cover. For the mantle and an overlying layer of water, arbitrarily chosen to be of 7 km, we use densities of 3.3 g/cc and 1.03 g/cc, respectively. Cohesion is set at c = 1000 Pa primarily to assure stability of steep slopes of near-surface sediments (<3 km), and the parameter has little influence at deeper levels of the crust, given the dominance of the frictional term. An internal friction angle φ = 27° in the crust, and a friction angle φ_b = 8° at the contact between overriding and subducting plates are low in order to include fluid pressure effects that are not accounted for explicitly, thus implying fluid pressure ratios within valid ranges at accretionary wedges (Fuller, 2006, and the references therein).

3.3 Model strategy

Our models simulate a transect along any accretionary margin that runs orthogonal to the main transport direction of the incoming material, where contractional structures develop. Although valid for accretionary subduction wedges elsewhere, we chose a model geometry and history that is comparable to the Anatolian subduction margin in Central Cyprus. We construct a Base Model in which the main parameters are the preferred values for the S-N transect along the Central Cyprus subduction (see Fig. 3). Subsequent models are presented as perturbations about this Base Model. Simulations are constrained by the present-day thickness and geometry of sedimentary units, and geological and plate-scale observations at the end of the simulation. However, off-section sources of material in the Anatolian margin, such as the mountainous areas to the north and northeast, and other potentially important three-dimensional effects that might occur in the area are not taken into account.

Our Base Model for Central Cyprus best represents the time evolution of crustal vertical motions since the Early Miocene along the transect. To select our Base Model, we attended to the overall agreement of large-scale structure evolution and vertical motions through time, as well as final geometry, with particular attention to the uplifted region and domains to the south and north of it. Based on our Base Model, the values of maximum sedimentation rate and viscosity for the parameter space have been selected through a model calibration procedure. We subsequently estimate the sensitivity of the model to changes in each parameter, which are presented as a set of model suites. In the Sedimentation Rate Suite, we study the effect of the selected value of the maximum sedimentation rate. In the Viscosity Suite, we study the rheological parameters of activation energy, Q, the power-law viscosity pre-exponential, A_μ and the power law exponent, n_μ, by systematically varying their values.

4. Results

4.1 Regional transect from the Mediterranean to Anatolia

We integrated tectono-sedimentary studies with our own data, and interpreted geophysical data from on- and offshore studies synthesized into crustal transects at 33º30' E (Fig. 3). Transect A in Fig. 3 spans from the African continental shelf to the Black Sea, and is a simplification of the lithospheric-scale transect shown in Stephenson et al., (2004). Crustal and upper-crustal cross-sections in panels B and C offer two original views of transects in Fernández-Blanco et al. (2020), which integrate and interpret geophysical studies in the area of interest.

To constrain the crustal geometries, we reconstruct sections at upper-crustal and full-crustal scale that span from the Eratosthenes Seamount, in the East Mediterranean Sea, to the interior basins of Central Anatolia. We use a collective interpretation of available geophysical data (e.g., Ergün *et al.*, 2005; Koulakov & Sobolev, 2006; Özeren & Holt, 2010; Mutlu & Karabulut, 2011) along a transect, which is integrated with the TransMed transect VII (Stephenson *et al.*, 2004), and accounts for tomographic constraints from Bakırcı et al. (2012) and Biryol et al. (2011). We reproduce the tectono-stratigraphy of Miocene and younger rocks and upper-crustal structures along the transect (Fig. 3C) integrating own findings (Fernández-Blanco *et al.*, 2013, 2019; Fernández-Blanco, 2014) with regional studies (Robertson, 1998a, 1998b; Harrison *et al.*, 2004; Stephenson *et al.*, 2004; Calon *et al.*, 2005a, 2005b; Çiner *et al.*, 2008; McCay & Robertson, 2013). We assembled the interpretation of these areas as shown in the original studies, and interested readers can find details there.

This integrative effort, which expands and is complementary to that presented in Fernández-Blanco et al. (2020), allows us to constrain four key features; (a) the shape of the subducting slab and the geometry of its contact with the continental crust; (b) the overall
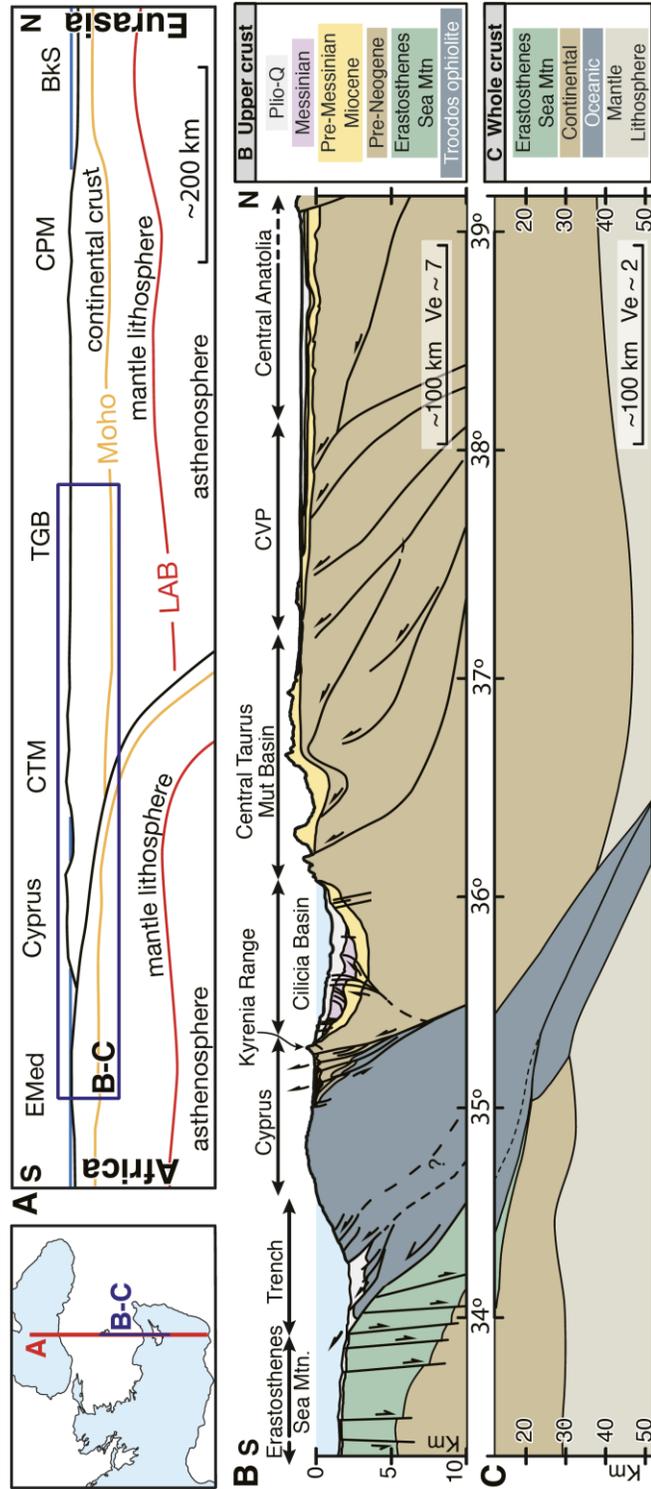
distribution of crustal thicknesses; (c) the relative age and cutting relationships of main structures, and; (d) the position, continuity and geometry of Miocene rocks.

The African plate, composed of the Eratosthenes continental fragment and surrounding oceanic crust, subducts northwards below the thickened continental crust in the south Anatolian margin. The Cyprus slab reaches an angle of ~45° at the contact with the base of the Anatolian crust and continues to steepen to the north (Fig. 3A, C). The overriding Anatolian lithosphere varies from ~110 km where its base contacts the slab, to ~85 km at the northern tip of the transect.

Crustal thicknesses vary along the transect (Fig 3C). In the African plate and in the southern end of the transect, changes in crustal thickness can be inferred from gravimetric anomalies (Ergün *et al.*, 2005) and models of the Moho depth (Koulakov & Sobolev, 2006). Crustal thicknesses have average values of ~28 km below the Eratosthenes Seamount and are minimum (~25 km) below the trench. Geophysical models show an increase in Moho depth northward, from ~28 km at 34°30'N to >40 km at 37° N, that we relate with slab steepening (up to 40°) (Fig. 3C). The slab maintains a similar dip until 36°30' N, where it steepens to ~60° north at ~60 km depth. This interpretation agrees with the presence of the slab at ~300 km depth farther north, as imaged in the section A-A of Biryol (2011). Maximum overriding crustal thicknesses of ~45 km at the point of contact between the African slab and the Anatolian Moho, below the Central Taurus Mountains, suggest crustal thickening in relation to subduction. We use the interpretation of Pn tomography inferring a decrease in crustal thickness to ~35 km in the Central Anatolian interior (Mutlu & Karabulut, 2011) over gravity data (Özeren & Holt, 2010) (Fig. 3E) suggesting a crust up to ~10 km thicker.

Figure 3. Transects along the Anatolian maring in Central Cyprus. Upper-crust and crustal-scale geological transects running N-S (650 km at around 33°30' E). The transects stretch from the Levantine Basin to the Tuz Gölü Basin across the Cyprus arc-trench, the island of Cyprus, the Cilicia Basin, the Central Taurus Mountains, and the Central Anatolian interior. The upper-left panel is a location map. Panel A is a transect across Central Cyprus and Anatolia, simplified from Stephenson et al. (2004), that has a topo-bathymetry with 3 times vertical exaggeration. EMed = East Mediterranean; CTM = Central Taurus Mountains; TGB = Tuz Golu Basin; CPM = Central Pontides Mountains; BkS = Black Sea. Panel B is the upper sector of the transect (up to 10 km depth), shown with vertical exaggeration of 7, and Panel C is the crustal cross-section for the area. These transects integrate upper crustal studies (Robertson, 1998; Stephenson et al., 2004; Calon et al., 2005a, 2005b; Çıner et al.,

2008; McCay, 2010; Fernández-Blanco et al., 2013) with the interpretation of several geophysical studies (Ates et al., 1999; Mart & Ryan, 2002; Ergün et al., 2005; Koulakov & Sobolev, 2006; Özeren & Holt, 2010; Mutlu & Karabulut, 2011; Abgarmi et al., 2017; Delph et al., 2017), as detailed in Fernández-Blanco (2014). CVP = Central Volcanic Province.

South-verging thrusts divide the area along the transect into present-day sedimentary basins and structural highs (Fig. 3B). The thrusts become older when progressing northward along the section, and have been linked with the Cyprian subduction megathrust, directly in the south (e.g., Stephenson *et al.*, 2004; Calon *et al.*, 2005a, 2005b) and indirectly in the north (Fernández-Blanco *et al.*, 2019). Thrusts are active at the trench (e.g., Stephenson *et al.*, 2004), Pliocene or younger in North Cyprus (e.g., McCay, 2010), mid-Pliocene in the Cilicia Basin (Aksu *et al.*, 2005), and pre-Miocene in the Mut Basin (e.g., Çiner *et al.*, 2008). Pliocene contractional structures are seen in the Cilicia Basin, but no evidence of any Miocene or younger thrust system is known for the Mut Basin or for the transition between both basins. This transition is marked instead by monoclinal flexure along a kink-band fold that accommodates ~4 km of relative vertical displacement between coeval Miocene rocks with minimum shortening (<1 %) (Fernández-Blanco *et al.*, 2019). The aforementioned evidence is compatible with tectonic forcing from the south and northward dissipation of strain across the subduction margin.

From south to north, Miocene rocks outcrop in four different localities: the Mesaoria Basin in Cyprus, the offshore Cilicia Basin, the Mut Basin on the Central Taurus Mountains, and the Tuz Gölü Basin, in the plateau interior (Fig 3B). Basin terminations in all four Miocene basins are erosive and controlled by post-depositional tectonic contacts, with the exception of the southern margin of the Mesaoria Basin, where these rocks pinch out. The middle and upper Miocene sequences infilling these basins are composed mostly of shallow-water limestones and thus allow for a first-order estimation of vertical kinematics relative to sea level since the end of the Miocene. Rocks above pre-Miocene substratum in the asymmetrical Mesaoria Basin thin southward and are disrupted to the north by the imbricate thrusts verging south that uplift the Kyrenia Range (Calon *et al.*, 2005a, 2005b; McCay, 2010). Contrarily, the transition between rocks at ~-2 km in the Cilicia Basin and at ~2 km in the Mut Basin is a broad monocline that occurs in the absence of surface-reaching faults

(Fernández-Blanco *et al.*, 2019). North of the Mut Basin, Miocene rocks in Central Anatolia are at relatively lower elevations (<1 km).

4.2 Base Model for Central Cyprus

Our Base Model uses a maximum sedimentation rate of 0.5 mm/y and viscous parameters values of Q = 170 kJ/mol, A_μ = 6.46 x 10^{-6} MPa^{-n}/s, and n_μ = 2.65. The complete list of parameter values used in our Base Model is shown in Table 1. Under a given strain rate, the crustal material of our Basic Model yields viscosities similar to those of quartzite, over a wide range of temperatures (see Fig. 4).
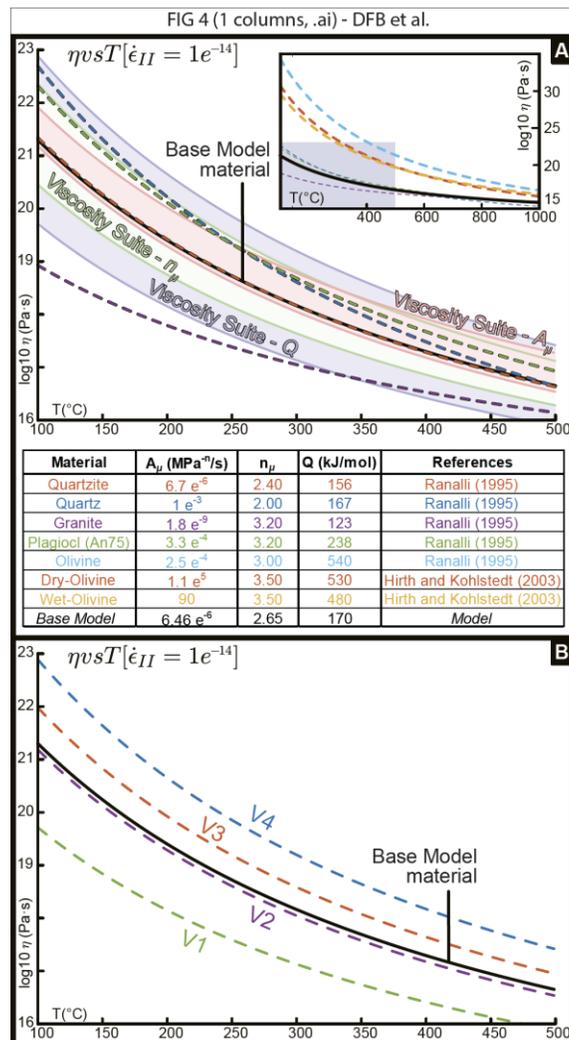

FIG 4 (1 columns, .ai) - DFB et al.

Material	A_μ (MPa^{-n}/s)	n_μ	Q (kJ/mol)	References
Quartzite	6.7 e^{-6}	2.40	156	Ranalli (1995)
Quartz	1 e^{-3}	2.00	167	Ranalli (1995)
Granite	1.8 e^{-9}	3.20	123	Ranalli (1995)
Plagiocl (An75)	3.3 e^{-4}	3.20	238	Ranalli (1995)
Olivine	2.5 e^{-4}	3.00	540	Ranalli (1995)
Dry-Olivine	1.1 e^{5}	3.50	530	Hirth and Kohlstedt (2003)
Wet-Olivine	90	3.50	480	Hirth and Kohlstedt (2003)
Base Model	6.46 e^{-6}	2.65	170	Model

Figure 4. Flow-law behavior of natural and simulated materials. *Plot of effective viscosity vs temperature for natural and modeled materials under a constant strain rate ($\epsilon = 10^{-14}$). Panel A shows the flow law behavior of olivine (+wet, +dry), in the upper right panel, as well as granite, quartz, plagioclase (An75) and quartzite (purple, blue, green and orange, respectively, in the main panel) alongside that of our Base Model material (black in both panels), and the ranges of parameter values in the viscous suites, which are shown in orange (for A_μ), in green (for n_μ) and in lilac (for Q) in the main panel. The table at the bottom shows the values and studies used. Panel B shows the flow law behavior of the models shown in Fig. 12; V1 (green); V2 (purple); V3 (orange); V4 (blue) and the Base Model material in black.*

The time evolution of the mechanical domain of the Base Model is shown in Fig. 5. The geometry of the mechanical domain at the moment of model initiation (25 Ma) has a roughly flat topography (Fig. 5A). In the model retro-wedge (right of the figure), we set a topographic barrier to confine the deposition of sediments within the model and avoid model instability. The curved geometry below the mechanical domain at the model pro-wedge (left of the figure) is set by the down-going slab, which is not shown in the figure.

At 10 My after model onset, a large forearc (negative-alpha) basin has developed (Fig. 5B). Horizontal isochrones cover the center and retro-wedge of the model. Topography has started to develop in the model pro-wedge in relation with two shear zones, marked by warmer colors in the second invariant of the strain rate. A small asymmetric wedge-top basin develops between the shear zones that is translated toward the retro-wedge (toward the right) as the shear zones migrate. The subducting slab becomes steeper, while the base of the crust becomes more horizontal. Both factors influence the extent of strain around the "S" point, at the base of the wedge.

After 15 Ma in model time, further deepening and thickening in the forearc basin leads to increasing strain accumulation, and temperatures, at the base of the crust (Fig. 5C). As the sediments accumulate in the forearc alpha-basin, the initial development of a frontal branch of a shear zone rooted at the "S" point leads the basement-basin contact to dip toward the model pro-wedge. As the model progresses, the wedge-top basin migrates towards the retro-wedge and the shear zones become wider and more pronounced. Another wedge-top basin starts to develop in the model pro-wedge.

Table 1. Main model parameters. *Values of the main parameters used for the Base Model, their associated references and comments on the value choice.*

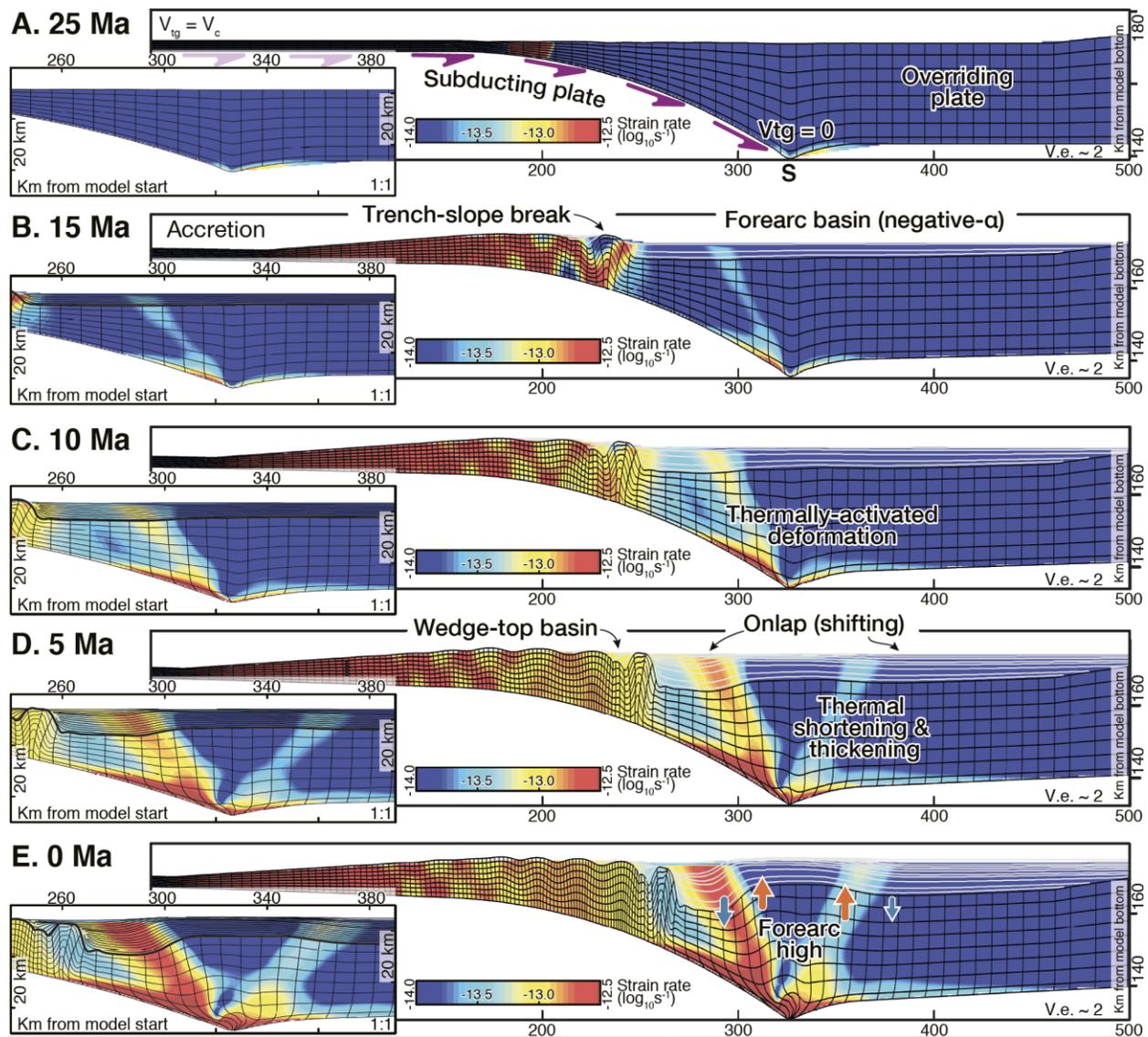|			Base Model for Central Cyprus	
			Mechanical Model	
Parameter	Description	Value	References	Comment
ρ_c	Crust density	2800 kg/m³	(Dziewonski & Anderson, 1981; Christensen & Mooney, 1995)	Generic crustal material composed of oceanic (3000 kg/m³) and continental crust (2700 kg/m³) and sediments between 1700 kg/m³ to 2650
ρ_m	Mantle density	3300 kg/m³	(Dziewonski & Anderson, 1981)	Includes the lithospheric mantle and asthenosphere
ρ_w	Water density	1030 kg/m³	(e.g., Nayar et al., 2016)	Sea water
ϕ	Internal friction angle	27°	(e.g., Davis et al., 1983; Flemings & Saffer, 2018)	
ϕ_b	Friction angle between subducting and overriding plate	8°		
c	Cohesion	1000 Pa	(e.g., Ikari & Kopf, 2011)	Should be between 1-10 MPa. Value used to sustain slope stability in sediments and avoid irrealistic failures affecting model stability. Value not affecting deeper sectors dominated by the friction component
D	Flexural rigidity	2.4 x 10²³ N·m	(Ranalli, 1995)	
S_a	Slab angle at S point	40°	(Fernández-Blanco et al., 2020)	Measured at the S point
v_c	Convergence velocity	35 mm/y	9.3 ± 0.3 mm/y in Cyprus (Reilinger et al., 2006)	Unrepresentative for 25 My. See explanation in main text
h	Sediment thickness in the subducting plate	3 km	Current thicknesses in East Mediterranean of 10-15 km (e.g., Makris & Stobbe, 1984)	Unrepresentative for 25 My. See explanation in main text
Sed_r	Sedimentation rate	0.5 mm/y		See explanation in main text
			Thermal Model	
Parameter	Description	Value	Reference	Comment
H_{sl}	Thickness of the subducting mantle lithosphere	70 km	(e.g., Pasyanos, 2010)	Commonly, 40-130 km
H_{ol}	Thickness of the overriding mantle lithosphere	80 km	(e.g., Pasyanos, 2010)	Commonly, 0-240 km
Ma_{lith}	Age of the subducting lithosphere	50 Ma	Debated	Assumed
t_{runup}	Thermal model run-up	20 My	(Robertson, 1998)	Retreat of the slab near to its present position at 25 Ma
$K_{l,a}$	Thermal conductivity (lithosphere, asthenosphere)	2.0, 50.0 W/(m·°K)	(Ranalli, 1995)	On the same order of magnitude
T_s	Surface temperature	27 °C		
T_a	Asthenosphere temperature	1400 °C	(Hofmeister, 1999)	
A	Heat production	0.85 μW/m³	(Jaupart & Mareschal, 2005)	
c	Specific heat	1200 J/Kg·°K	(Turcotte & Schubert, 2002)	
A_μ	Power-law viscosity coefficient	6.46 x 10⁻⁶ MPa⁻ⁿ/s	(Ranalli, 1995)	See also Supplementary Fig. X
n_μ	Power-law viscosity exponent	2.65	(Fernandez-Blanco et al., 2020)	See also Supplementary Fig. X
O	Activation energy	170 kJ/mol		See also Supplementary Fig. X

Figure 5. Base Model. *Mechanical model evolution in time steps, with zoom-ins into the area where the forearc high develops. Times represented are, from top to bottom: 25Ma, 15Ma, 10Ma, 5Ma, and present. Strain rate is shown in vivid colors ranging from blue (low; -14.0 log₁₀ s⁻¹) to red (high; -12.5 log₁₀ s⁻¹). The mesh of black lines records cumulative deformation in the basement since model onset. The individual lines on top of the basement (white in main panels and black in zoom-in views) represent isochrones of deposited and subsequently deformed sediment.*

At 20 Ma, two shear zones branch out from the "S" point and produce a broad uplifting bulge above it, in the central-right area of the model (Fig. 5D). The shear zones delimit the uplifted area of the forearc high, which dips gently toward the left side of the model. The basement further tilts pro-wedge ward (left), and isochrones mark the onset and

development of a monoclinal fold. Overall, horizontal isochrones on top of the bulge transition to isochrones dipping away from the bulge to its sides creating a broad anticlinorium. Onlap relationships take place on both sides of the bulge with larger angles in the model pro-wedge.

At the end of the model run, during the last 5 Ma, vertical motions in the forearc are prominent (Fig. 5E). The bulge divided the forearc basin in two, a pro- and a retro-wedge sub-basin, sea- and land-wards respectively, and onlap relationships to its sides develop further. The deflection of the slab proceeds toward higher angles (~40°) at the "S" point and the base of the wedge has smaller angles farther toward the retro-wedge. The basement of the pro-forearc basin deepens while uplift continues in the forearc high. An area with low values in the second invariant of strain rate develops in the uppermost ~5 km of the forearc high.
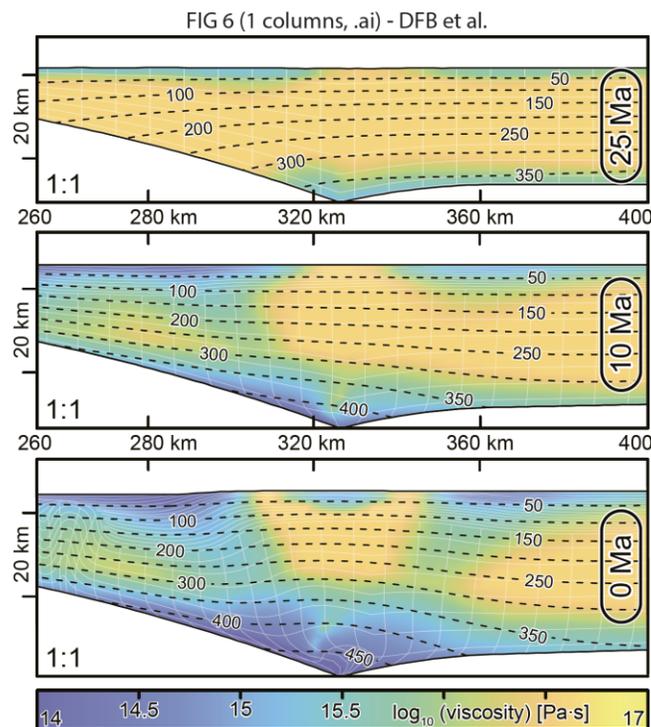
Figure 6. Temperature, viscosity, and deformation during forearc high growth. *Correlation among temperature (in °C, shown as black dashed lines), viscosity (in Pa·s, shown as gradient colors between blue -low- and yellow -high-), and the deformation mesh of the mechanical model (as a grid for the basement and originally-horizontal isochrones for the sedimentary cover, both in light white) in the area where the forearc high develops in 3 time steps: 25Ma, 10Ma, and present.*

4.3 Sedimentation Rate Model Suite

Sedimentation in the models is "fill-to-spill" and areas between structural highs that are capable of accommodating sediments are filled to capacity. In doing this, we assume the availability of sufficient sediment throughout the model run. We set each model with a different maximum sedimentation rate that remains constant throughout the model run (Tables 1 and 2, and Fig. 7).

Models show that as the maximum sedimentation rate increases, the strain becomes greater in and around the "S" point and is distributed in shear zones to its sides. The subducting lithosphere becomes steeper toward the model retro-wedge while the base of the crust further deflects toward the "S" point. This is, increasing sedimentation leads to an "S" point that subsides relative to the geoid. However, whereas models with more sediment in the system show a decreasing surface uplift, models with a higher maximum sedimentation rate that surpasses a threshold, exhibit larger surface uplift (see videos Sr0 to Sr12 in supplementary materials).

As sedimentation increases, thicker forearc basins develop that tend to stabilize the margin and translate deformation towards the basin margins. This leads to limited forearc uplift (Fig. 7, right). The uplifted region above the thermally-activated viscosity becomes broader, and the points of maximum uplift and maximum deposition move landward (see videos Sr8 and Sr10 in supplementary materials). Similarly, vertical displacements are smaller. This is recorded as angular discordances in the basin chronolines, showing onlap relationships in models with faster forearc high growth. Increasing sedimentation also results in relative vertical displacements between subsided and uplifted areas that are consistently larger and occur in narrower (horizontally shorter) distances, i.e. larger amplitudes in the main subsidence-uplift pair (forearc high - pro-basin).

	Model run name	Sedimentation rate (mm/yr)	Power-law viscosity A_μ (x10^{-6} MPa^{-n}/s)	n_μ	Activation Energy Q (kJ/mol)	Video in figs or suppl. material?
	Base Model	0.5	6.46	2.65	170	**Figs. 4-10 & 12**
Sedim. Rate Suite (constant per model)	Sr0	0.0	6.46	2.65	170	**Fig. 12 & Vid. Sr0**
	Sr1	0.1	6.46	2.65	170	**Figs. 7**
	Sr2	0.2	6.46	2.65	170	**Vid. Sr2**
	Sr3	0.3	6.46	2.65	170	**Fig. 12**
	Sr4	0.4	6.46	2.65	170	**Vid. Sr4**
	Sr5	0.5	6.46	2.65	170	**Base Model**
	Sr6	0.6	6.46	2.65	170	**Vid. Sr6**
	Sr7	0.7	6.46	2.65	170	**Fig. 12**
	Sr8	0.8	6.46	2.65	170	**Vid. Sr8**
	Sr9	0.9	6.46	2.65	170	**Figs. 7**
	Sr10	1	6.46	2.65	170	**Fig. 12 & Vid. Sr10**
	Sr11	1.1	6.46	2.65	170	
	Sr12	1.2	6.46	2.65	170	**Vid. Sr12**
	Sr13	1.3	6.46	2.65	170	
Viscosity Suite (values at model onset)	A1	0.5	0.15	2.65	170	
	A2	0.5	2.37	2.65	170	**Fig. 8 & Vid. A2**
	A3	0.5	4.26	2.65	170	
	A4	0.5	6.46	2.65	170	**Base Model**
	A5	0.5	8.27	2.65	170	
	A6	0.5	10.88	2.65	170	**Fig. 8 & Vid. A6**
	A7	0.5	13.09	2.65	170	**V3 in Fig. 4 & 12**
	n1	0.5	6.46	2.35	170	
	n2	0.5	6.46	2.45	170	**Fig. 9 & Vid N2 V2 in Figs. 4 & 12**
	n3	0.5	6.46	2.55	170	
	n4	0.5	6.46	2.65	170	**Base Model**
	n5	0.5	6.46	2.75	170	
	n6	0.5	6.46	2.85	170	**Fig. 9 & Vid. N6**
	n7	0.5	6.46	2.95	170	
	Q1	0.5	6.46	2.65	140	**V4 in Figs. 4 & 12**
	Q2	0.5	6.46	2.65	150	**Fig. 10 & Vid. Q2**
	Q3	0.5	6.46	2.65	160	
	Q4	0.5	6.46	2.65	170	**Base Model**
	Q5	0.5	6.46	2.65	180	
	Q6	0.5	6.46	2.65	190	**Fig. 10 & Vid. Q6**
	Q7	0.5	6.46	2.65	200	**V1 in Figs. 4 & 12**

Table 2. Models and parameterization. Models used in this study, the values of the four parameters that are changed systematically for the maximum sedimentation rate and viscosity suites, with reference to figures and videos of some representative simulations.
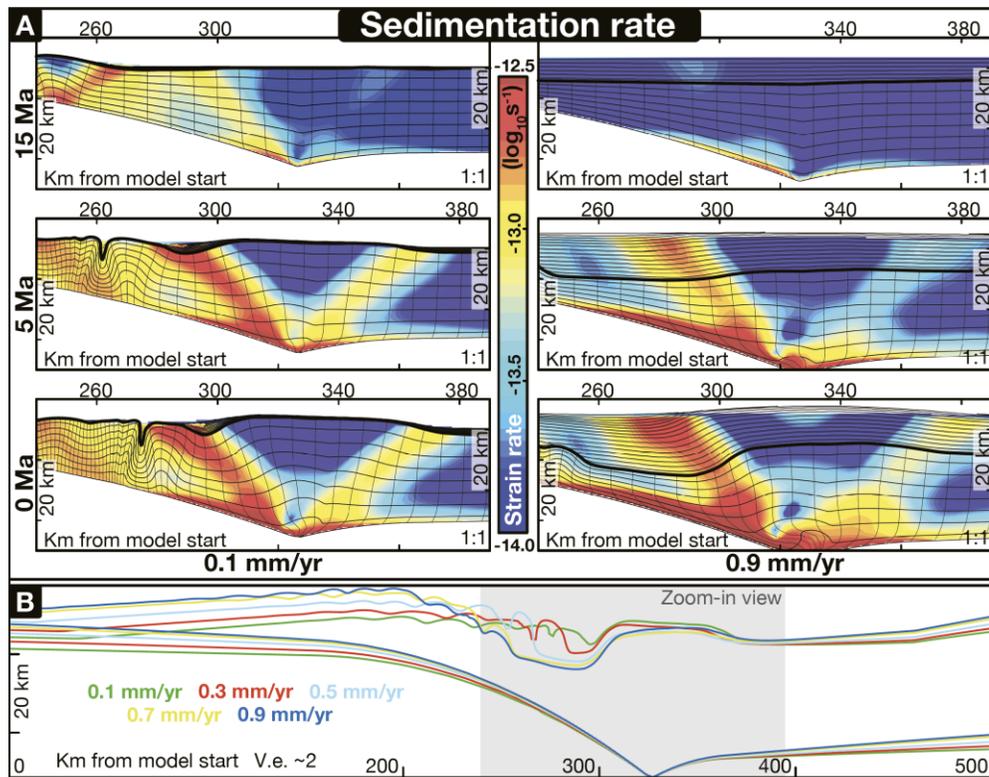
Figure 7. Variations in maximum sedimentation rates. Forearc high development with changes in maximum sedimentation rate. A) The figure shows models at 15 Ma, 5 Ma, and 0 Ma and includes an inset of the model where the forearc high develops, for the models with 0.1 mm/y (left column) and 0.9 mm/y (right column). The individual back lines on top of the basement represent isochrones that reflect deformation since their successive inception in time, and thus the overall geometric relationships expected for strata. A thicker black line marks the basement-infill contact. The dimmed grey box shows the approximate location of the zoom-in view. B) Line trace of the bottom of the crust and top of the basement in models with changes in sedimentation rates after a complete run. Vertical reference frame is taken from the "S" point at the base of the crust. Upper panels are at 1:1 scale and the bottom panel is at 1:2 scale.

With low maximum sedimentation rates (Fig. 7, left), the initial forearc basin is thin and imposes no restrictions to forearc high surface uplift, which occurs earlier with respect to model onset, i.e. forearc high is older, and both downward/upward vertical motions take place over shorter periods (see videos Sr2 and Sr4 in supplementary materials). In general, with lower sedimentation rates the margin is more susceptible to the influence of the other parameters; for example, the incoming sediment at the trench markedly affects the structural evolution of the margin, which exhibits sharper shear zones that migrate toward the retro-wedge of the model faster and structural highs and lows that are larger in amplitude.

4.4 Viscosity Model Suite

The combination of parameters in Eqn. (1) determine the effective viscosity of a thermally-activated viscous material, defined as the proportionality constant between strain rate (D_{ij}) and stress (σ_{ij}). With a non-linear stress dependence, the relationship is complicated, but for a given stress level, the effective viscosity determines whether or not the material will flow at a significant rate (see Fig. 4) over the geologic timescale of interest. By changing these parameters, we can investigate how changes in the effective viscosity affect deformation in the deep wedge. As a general principle, any decrease in the effective viscosity encourages flow of the deep crust, and under horizontal compression, leads to crustal thickening and forearc uplift. Tables 1 and 2, and Fig. 4 show the range of values explored.

The pre-exponential viscosity parameter A_μ directly scales the effective viscosity, and thereby becomes an explicit control on forearc deformation. Within the parameter range investigated (Tables 1 & 2; Fig. 4), lower values produce a deeper initial forearc basin, but delays the time of formation of the forearc high with respect to our Base Model. A_μ affects the amount of relative differential motion between the subsiding and the uplifting sectors of the forearc high and the age of the motions. Forearc high growth cannot counteract the primary subsidence signal (Fig. 8, left). Subsidence in the initial forearc basin decelerates with time until the formation of the structural high leads to accelerating subsidence in the pro-basin and protracted decelerating subsidence in the retro-basin (see video A2 in supplementary materials). Higher values of A_μ result in the rise of pronounced forearc high that develop in relation to broader shear zones, i.e. more diffuse strain, and at earlier times than our Base Model. Forearc high formation outpaces the primary subsidence signal imposed by sediment loading and surface uplift in the forearc high area is eventually larger than the subsidence recorded since forearc basin onset (Fig. 8, right). The rate of the motions after forearc high development accelerates with time in both forearc high and pro-forearc basin, resulting in differential motions that become larger with time in the forearc high pro-wedge, in contrast

to its retro-wedge, where the rate of subsidence remains roughly constant (Fig. 8; video A6 in supplementary materials).
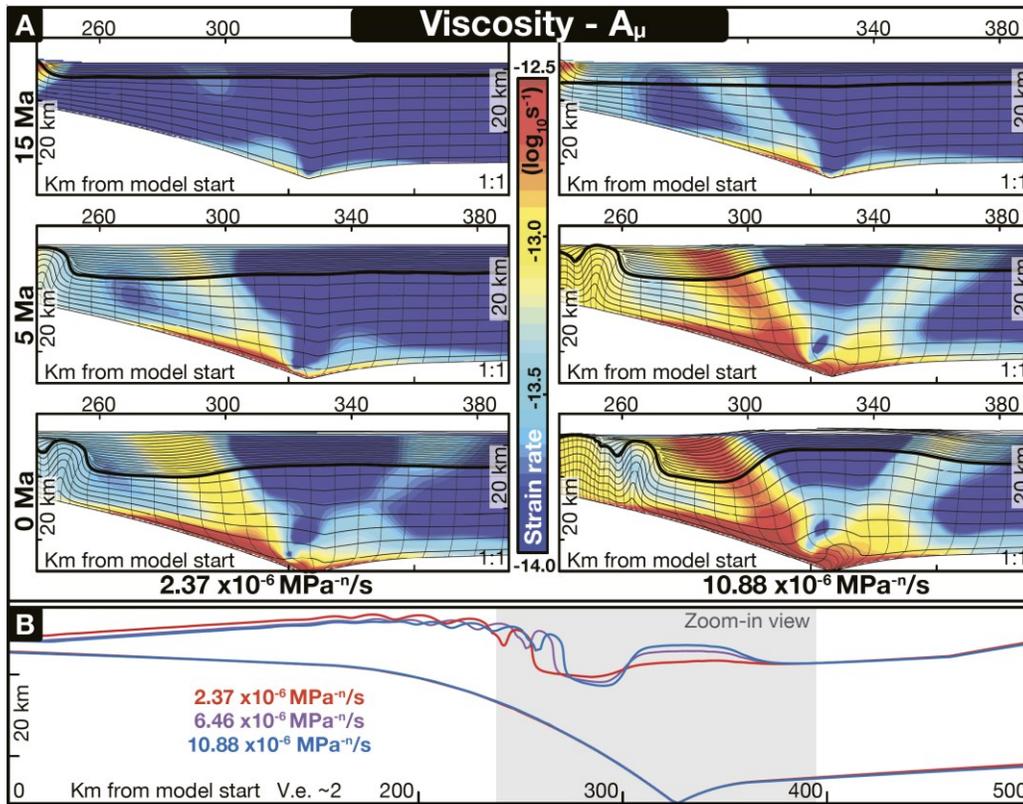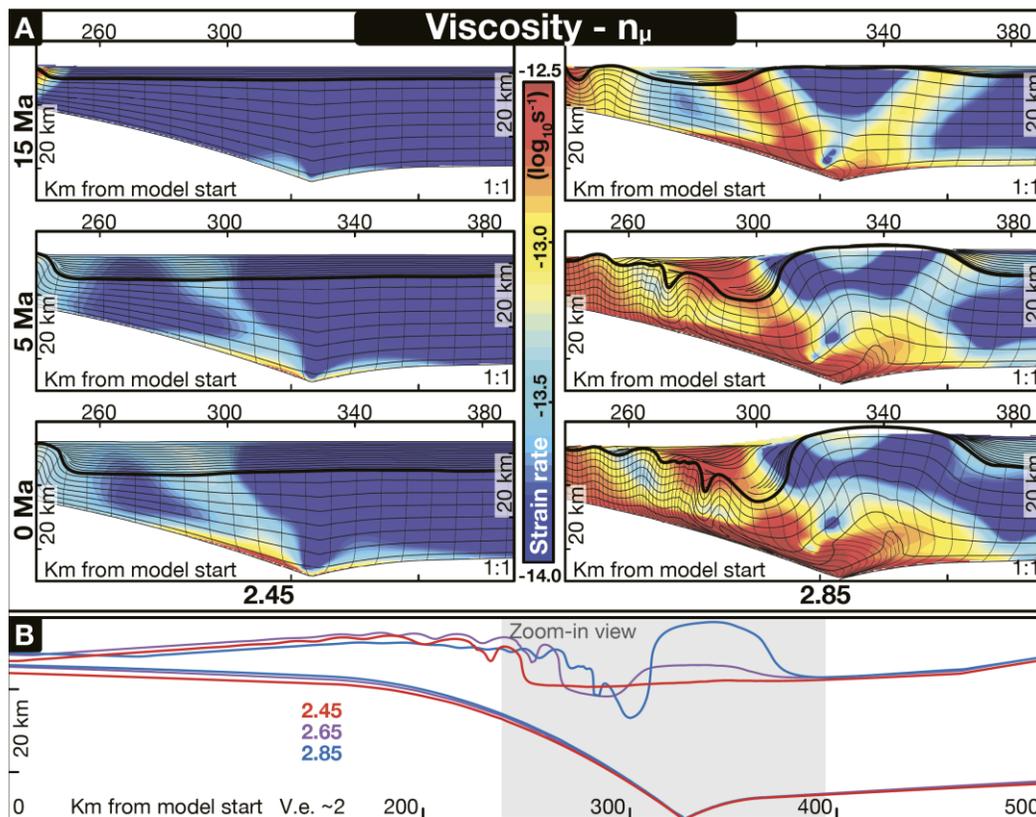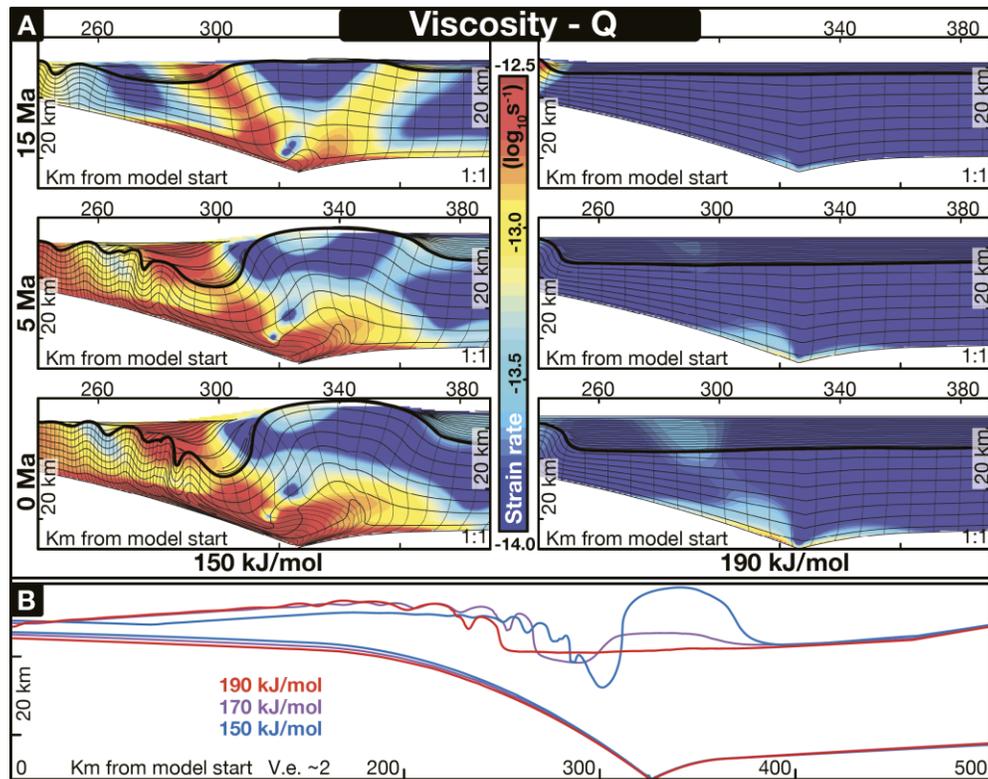

Figure 8. Variations in A_μ. *Forearc high development with changes in the viscosity parameter Aμ. A) The figure shows 15 Ma, 5 Ma, and 0 Ma snapshots of an inset of the model where the forearc high develops, for the models with 6.46×10^{-6} MPa^{-n}/s (left column) and 13.09×10^{-6} MPa^{-n}/s (right column). The individual back lines on top of the basement represent isochrones that reflect deformation since their successive inception in time, and thus the overall geometric relationships expected for strata. A thicker black line marks the basement-infill contact. The dimmed grey box shows the approximate location of the zoom-in view. B) Line trace of the bottom of the crust and top of the basement in models with changes in the value of the viscosity parameter Aμ after a complete run. Vertical reference frame is taken from the "S" point at the base of the crust. Upper panels are at 1:1 scale and the bottom panel is at 1:2 scale.*

The parameter n_μ exerts a control on the age, wavelength, and rate of the relative differential motions in the forearc high area, as it does on strain localization. Changes in n_μ result in a different average viscosity, so the behaviour is similar to A_μ, but it also has effects through the greater strain localization that occurs with a higher exponent. Lower values of n_μ within the parameter spectrum studied (Tables 1 & 2; Fig. 4) result in the onset and protracted development of the initial forearc basin that thickens at a decelerating rate of

subsidence (Fig. 9, left). The protracted growth of the initial forearc basin renders difficult the surface uplift of the forearc high, which cannot outpace subsidence (see video n2 in supplementary materials). Higher values of n_μ produce an early uplift at older times than our Base Model. The forearc high forms soon after the model onset, dividing an underdeveloped initial forearc basin. Uplift rates accelerate with time in the forearc high and its width remains roughly constant (Fig. 9, right). While the subsidence rates in the pro-wedge basin initially accelerate and then slow down at younger times, the retro-basin records the opposite trend in subsidence rates, with an older deceleration and a younger acceleration (Fig. 9; video n6 in supplementary materials).

Figure 9. Variations in n_μ. Forearc high development with changes in the stress exponent of viscosity, nμ. A) The figure shows 15 Ma, 5 Ma, and 0 Ma snapshots of an inset of the model where the forearc high develops, for the models with 2.45 (left column) and 2.85 (right column). The individual back lines on top of the basement represent isochrones that reflect deformation since their successive inception in time, and thus the overall geometric relationships expected for strata. A thicker black line marks the basement-infill contact. The dimmed grey box shows the approximate location of the zoom-in view. B) Line trace of the bottom of the crust and top of the basement in models with changes in the value of the viscosity parameter nμ after a complete run. Vertical reference frame is taken from the "S" point at the base of the crust. Upper panels are at 1:1 scale and the bottom panel is at 1:2 scale.

Within the parameter spectrum investigated (Tables 1 & 2; Fig 4), the activation energy, Q, influences the occurrence and shape of uplift in the forearc high. Relatively low values result in a lower average effective viscosity that leads to an uplift that is larger and occurs at earlier stages than in our Base Model. Uplift of a convex up area blocks the development of the initial forearc basin while inducing a second uplift in the model retro-wedge (Fig. 10, left). Surface uplift in the forearc high outpaces the primary subsidence, and uplift rates accelerate with time. Subsidence rates in the forearc lows to the sides of the forearc high also accelerate with time (see video Q2 in supplementary materials). The width of the pro-basin decreases with time while that of the retro-basin increases until it stabilizes. Higher Q values accelerate the subsidence rates in the initial forearc basin, as the basin becomes slightly narrower. Higher Q values effectively negate the thermal activation mechanism, thus viscosity remains low, and deformation under the forearc basin is almost fully inhibited (Fig. 10, right). Even with an underfilled forearc basin, deformation never propagates landward of the active, critical wedge, and never approaches the S-point at the upper plate contact (Fig. 10, right; video Q6 in supplementary materials).

Figure 10. Variations in Q. Forearc high development with changes in the activation energy, Q. A) The figure shows 15 Ma, 5 Ma, and 0 Ma snapshots of an inset of the model where the forearc high develops, for the models with 150 kJ/mol (left column) and 190 kJ/mol (right column). The individual back lines on top of the basement represent isochrones that reflect deformation since their successive deposition in time, and thus the overall geometric relationships expected for strata. A thicker black line marks the basement-infill contact. The dimmed grey box shows the approximate location of the zoom-in view. B) Line trace of the bottom of the crust and top of the basement in models with changes in the value of the viscosity parameter Q after a complete run. Upper panels are at 1:1 scale and the bottom panel is at 1:2 scale.

5 Discussion

Models in this paper are based on the mechanism of forearc high uplift by deep crustal flow presented by Fuller *et al.* (2006a), expanded and applied to the Anatolian margin by Fernández-Blanco *et al.* (2020). In these models, sediment accretion and syn-accretion sedimentation in the forearc basin lead to higher temperatures at deeper levels of orogenic wedges. Increased temperatures change the deformation mechanics in the lower crust from brittle to viscous. Thermal weakening of the lower crust results in ductile flow, and thickening and shortening of the wedge that leads to the dynamic growth of the forearc high through sustained accretionary growth. Models in this paper show how the sedimentation rate in the forearc basin, the rheological characteristics of the crust, and the initial thermal and viscous state of the wedge control the timing and geometry of early large-wavelength subsidence and subsequent short-wavelength uplift-subsidence of the forearc high-seaward basin pair.

5.1 Thermo-viscous uplift and forearc high growth

Subduction geometry and rheological parameters set the orogen cross-sectional shape, and the non-linear growth of topography at the wedge rear. In the convergence direction and sense, the orogen has a critical, positive-alpha topography from trench to trench-slope break, followed by a stable or critical, negative-alpha topography at the front of a forearc high (Fuller *et al.*, 2006a; Willett & Schlunegger, 2010; Fernández-Blanco *et al.*, 2020). Arcward of the forearc high, the wedge is argued to be subcritical and the growing wedge taper is maintained by sedimentation rather than deformation. When the available accommodation space is filled with sediments, a wide negative-alpha basin develops that halts strain in the underlying wedge and sustains stable-wedge sliding above the decollement (Fuller *et al.*, 2006a; Willett & Schlunegger, 2010). In the negative-alpha basin, sediment thickness and thermal resistivity contribute to increased temperatures and the activation of viscous flow in the lower crust, leading to shortening, thickening and uplift of a forearc high in the rear of wedges under compression (Fernández-Blanco *et al.*, 2020). Such a thermo-viscous forearc high is not growing to maintain self-similar wedge geometry, but rather has high strain rates and rises faster than surrounding areas forming a structural culmination.

Our simulations suggest that forearc highs can grow without a material-strength backstop, solely as a function of the geometrical characteristics of the slab and wedge itself, and as controlled by dynamic effects and feedback among several processes. The geometry and dip of the subducting slab controls where sediment is detached from the oceanic plate and accreted into a critical wedge. Geometry, in particular the curvature of the slab, determines where and if the overriding wedge shifts from critical to stable. This shifting point, at the transition between the critical, deforming wedge and the forearc basin where sedimentation stabilizes the wedge, sets the location of the initial forearc high. The late stage forearc high that develops in response to thermal activation of crustal flow initiates landward of this point, where sediment blanketing leads to high temperature. Models show

that the uplift of the forearc high occurs for a wide range of values of thermal conductivity, viscosity and sedimentation rate, and becomes more probable with time, as the forearc system enlarges and becomes more mature (Fernández-Blanco *et al.*, 2020). The thermal structure of the deep wedge is key, for it facilitates or hinders viscous deformation. If accretionary flux and convergence velocity are continuous and sufficient, a thermally activated viscosity drop at the base of the crust results in coupled, counteracting uplift and subsidence at the surface. The aforementioned inferences imply that forearc highs may not be considered an isolated feature conditioned to backstop presence (e.g., Byrne *et al.*, 1993), but rather an integral part of accretionary wedges that develop at advanced stages of wedge growth (e.g., Pavlis & Bruhn, 1983) as a function of the accretionary flux, initial wedge viscosity and synorogenic sedimentation.

5.2 Synorogenic sedimentation controls on forearc high growth

Variations in sedimentation rate significantly influence the growth of the margin (Fig. 7). Synorogenic sedimentation and growth of the main forearc basin increase the temperature of the lower crust through the thermal resistance of the sedimentary pile. The increased thickness of the overburden increases the temperature of the underlying crust, and if the sediments have low thermal conductivity, this "thermal blanketing" effect becomes more prominent. The effect is transient; while the low temperature of basinal sediments tends to lower the geothermal gradient, the gradient is eventually restored by diffusive heating in the basin, which results in high temperatures in the lower crust.

Sedimentation and deformational crustal thickening both contribute to progressive thermal activation of ductile strain in the lower crust, and ultimately propel the growth of a forearc high. When sediment input is small, there is no sediment loading of the critical accretionary wedge and the resultant deformation leads to the development of structural highs along the margin. A broad forearc high develops with small flanking basins (Fig. 7, left).

As sedimentation increases, a long wavelength subsidence takes place at model initial stages and the onset of the forearc high growth is delayed (Fig. 7, right). Models with higher maximum sedimentation rate have a larger sediment load and thus suppress deformational growth of a forearc high, and retain protracted long-wavelength subsidence.

Our models of accretionary margins show that if the amount of incoming sediments at the trench remains constant, variations in the sedimentation rate control the growth rate and thus the occurrence of surface uplift in the forearc high regions. With a high sediment flux and large accommodation space, the mass flux by sediment deposition can be the largest flux in the system. These results lead to the counterintuitive postulation that regional subsidence in the forearc basin can be the main cause behind surface uplift in a new forearc high internal to the basin.

5.3 Wedge rheology controls on forearc high growth

Variations in initial wedge viscosity markedly influence the growth of the margin (Fig. 8 to 10). Wedge viscosity and its thermally-controlled dynamic state lead to different degrees of strain localisation that in turn control the occurrence, age, wavelength and rate of uplift in the wedge. Higher initial wedge viscosities, achieved through some combination of low A_μ, low n_μ and/or high Q, limit the viscous flow, delaying or preventing the uplift of the forearc high, and lead to stable wedges that widen and thicken only by sedimentation and subsidence in the forearc. On the contrary, under the same accretionary flux, lower initial wedge viscosities, achieved through some combination of high A_μ, high n_μ and/or low Q, facilitate ductile flow and the uplift of the forearc high by shortening and thickening. We thus infer that low viscosity at initial stages of wedge growth have similar effects as high temperatures in the evolution of the internal sectors of the wedge, and both parameters act to accelerate the morphologic evolution of mature wedges.

As suggested by previous studies (Vanderhaeghe *et al.*, 2003), lowering the initial viscosity of the wedge results in larger decoupling of the lower crust, and increasing the extent of the viscous flow landwards. Our models further suggest that this effect is to a large extent controlled by syn-accretion sedimentation. Lower initial wedge viscosity results in a broader and more pronounced forearc high, sharply bounded by a seaward and a landward basin that continue to subside by sedimentary load. Sedimentation in these bounding forearc lows control the extent of viscous flow, and thus that of the uplift in the forearc high. Accommodation space in the negative-alpha basin at the front of the forearc high is controlled by the high in its proximal basin edge and by tectonic uplift of the slope-trench break in its distal basin edge (Willett & Schlunegger, 2010). On the contrary, accommodation space in the forearc basin at the back of the forearc high is solely controlled by the forearc high. As a result, accommodation space increases at a faster pace in the seaward basin, in turn leading to an extra sedimentary load that translates the viscous flow of the lower crust farther landward. This effect, facilitated by lower viscosity and larger decoupling of the negative-alpha region, increases the volume of viscously deforming rock in the lower crust and leads to lateral growth of the forearc high into a plateau.

5.4. Coupled control of sedimentation and viscosity on forearc high growth

The interplay between sedimentation and viscosity is illustrated by the range of models presented in this paper and summarized in Fig. 11. Although specific rheological parameters affect deformation differently, the first order effect of rheology can be expressed through an average effective viscosity of the lowermost crust of the upper plate, where deformation through thermal activation initiates (Fernández-Blanco *et al.*, 2020). Models in Fig. 11 show the influence of viscosity on structural style, from early, intense crustal thickening and forearc uplift with a localized forearc basin (Fig. 11, lower left) to a broad basin blanketing both upper plate, slab and the interface, without deformation in the lower crust (Fig. 11,

upper right). In this latter example, material is too strong or too cold to sustain deformation, despite thermal effects of sediment deposition. The end result is a wide, negative-alpha basin with no mechanical backstop supporting the critical wedge (Fig. 11, upper right). In the opposite extreme (Fig. 11, lower left), the crust is very weak, deformation is extensive throughout the forearc, and basins are small and structurally controlled. The accretionary wedge backthrusts over the upper plate upper mantle, which subsequently acts as a low-angle mechanical backstop.

The sedimentation effect is more subtle as it depends on the interplay with the rheology (Fig. 11, upper left to lower right diagonal). For most of the rheology models considered in this contribution, high sedimentation leads to thermal weakening and broad zones of deformation (Fig. 11, lower right). Low sedimentation produces a smaller loading effect on the critical wedge that leads to brittle-dominated deformation that spans a broader zone, even in the absence of thermally-activated viscous deformation (Fig. 11, upper left). Between end-member models, when sedimentation is sufficient to suppress brittle deformation and insufficient to increase temperatures, minimal deformation results in models that appear much like the strong rheology case, shown in the upper right.

Figure 11. Sedimentation rate and viscosity controls on wedge and basin morphology. Changes in wedge morphology and basin architecture as a function of maximum sedimentation rate and crustal viscosity shown along two axes that cross on the Base Model. The top-left to bottom-right diagonal shows models with varying sedimentation rates between 0 mm/yr in the top-left and 10 mm/yr in the bottom-right, with a fixed rheology model (Base Model -Fig. 4). The bottom-left to top-right diagonal shows models as a function of rheology, parameterized by effective viscosity at a strain rate of 10^{-14} with log viscosity values varying from 14.48 Pa·s (at 350°C) in bottom-left to 16.38 Pa·s (at 350°C) in the top-right. Effective viscosity models, V1 to V4, are shown in Fig. 4B. Light white lines show the deformation mesh of the mechanical model. A grid represents the basement and originally-horizontal lines are isochrones for the sedimentary cover, and their contact (top of the basement), is shown with thicker stroke. Isotherms are in dashed black lines, with numbers in °C. Figure shows the model sectors with morphological variations, between 150 km and 500 km, and excludes far sides, where wedge morphology is similar.
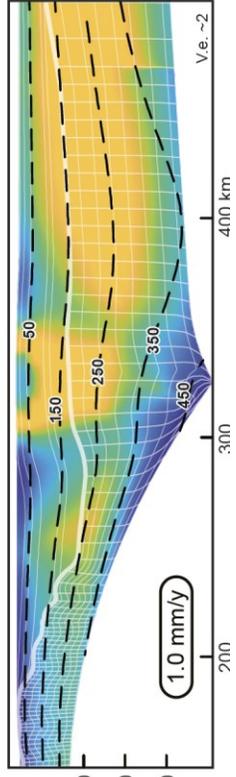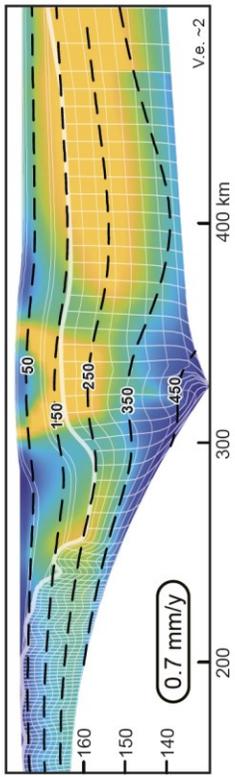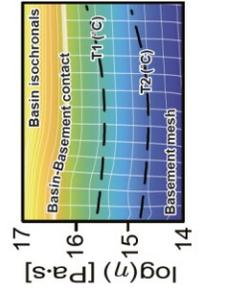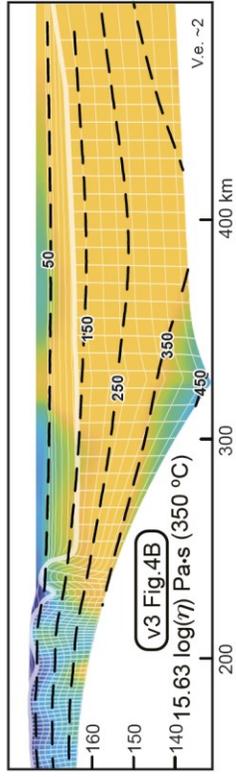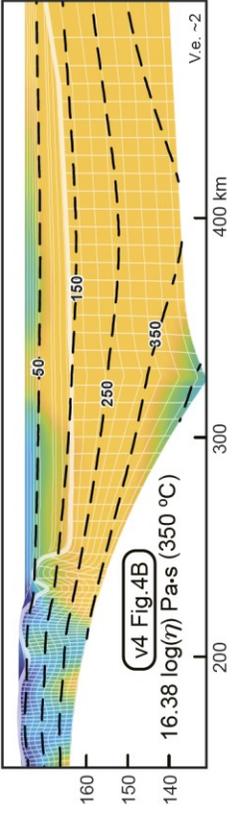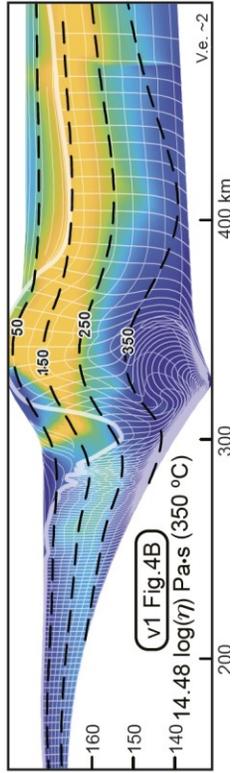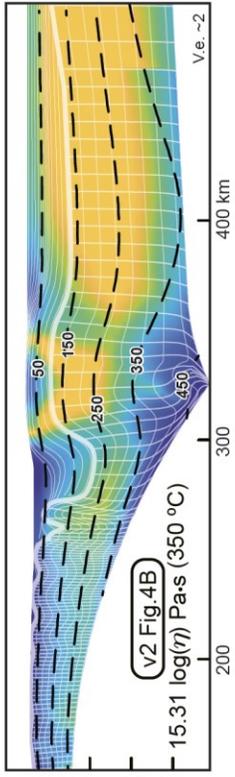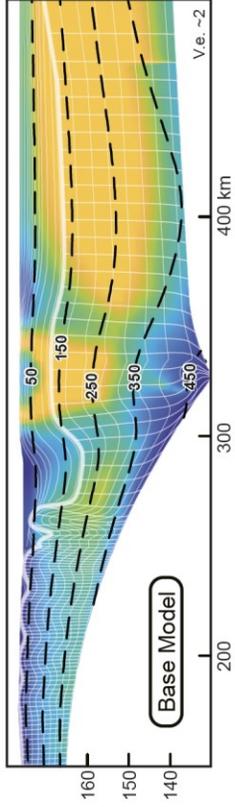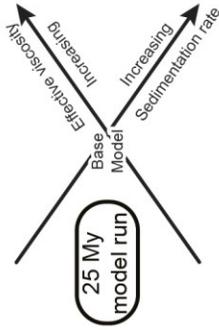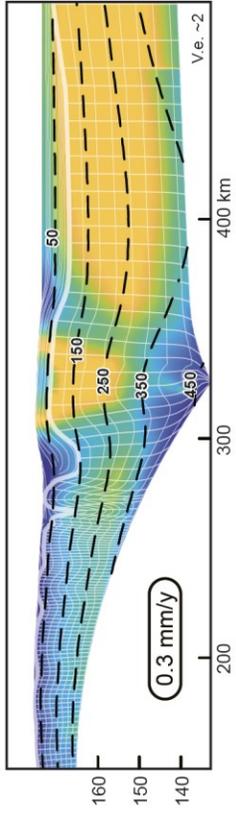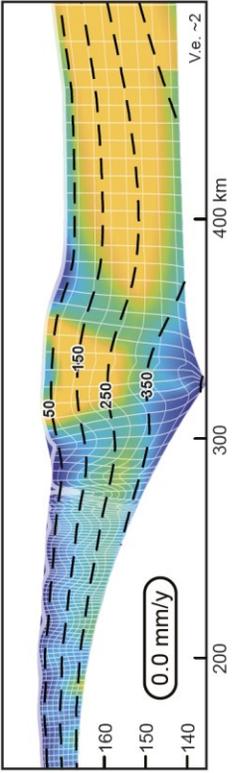
Forearc high growth thus interacts with sedimentation through two competing processes. First, sedimentation provides a mechanical load to the accretionary wedge, determining whether the wedge deforms critically, and uplifts the forearc high, or is held in a sustained sub-critical or stable state with no internal deformation. Second, the sediments deposited in a wedgetop or forearc basin act as a thermal insulator that heats the underlying crust and eventually leads to thermal weakening, thereby increasing deformation, including uplift. Therefore, sedimentation can either suppress deformation (loading) or increase deformation (heating). It is thus not surprising that the response to sedimentation is highly complex and nonlinear, and that a varied set of structures and basin architectures develop depending on the interplay between deformation and sedimentation (Fig. 11).

5.5. The Anatolian margin and the forearc high uplift in South Turkey

The analysis of the structures observed along the regional 2D geologic transect of the central Cyprus arc suggests shortening from the trench to south Turkey (Fig. 3). The type, distribution, relative age, and geometry of these contractional structures are compatible with their development in relation to a wide accretionary subduction system (e.g., Dickinson & Seely, 1979) (Fig. 1). Our simulations can reproduce the overall geometry and the main contact relationships as well as the main vertical tectonic events of the south Anatolian upper plate and are also consistent with other geologic observations. These include early continuity and later disruption of Miocene basins in the presence of brittle, regional-scale accommodating structures in the seaward regions, i.e., the trench, the trench-slope, and the trench-slope break areas, and broad monoclinal flexure above ductile strain in the otherwise largely undeformed landward forearc basin region (Figs. 1, 3, 5) (Fernández-Blanco *et al.*, 2020). Therefore, mechanical accretion from Cyprus dominates deformation in the Mesaoria Basin and the Kyrenia Range, in Central Cyprus, while ductile deformation at deeper levels

controls the growth of the Central Taurus Mountains, in south Turkey, and thus the evolution of the basins of Cilicia and Mut (Figs. 1 & 12).
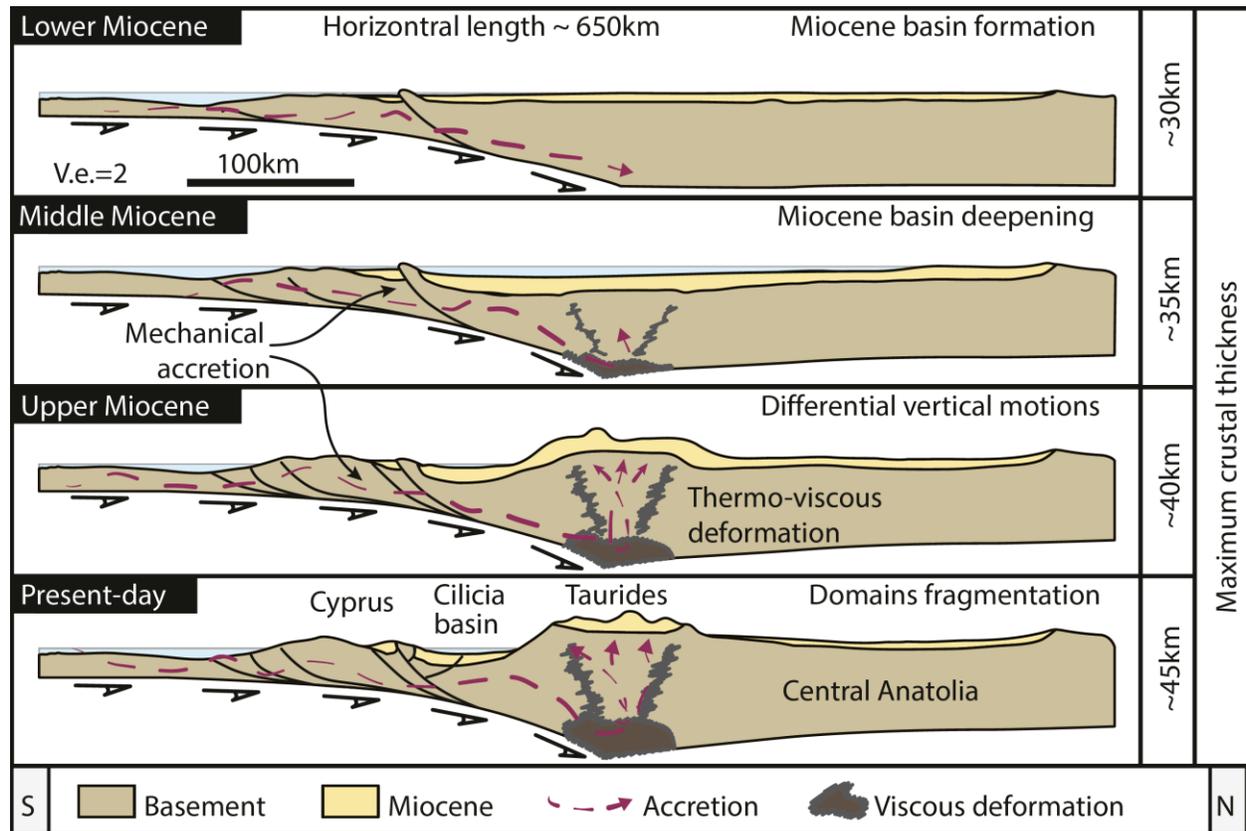

Figure 12. Conceptual evolution of the Anatolian margin in Central Cyprus.

South Turkey surface uplift and growth of the modern Central Taurus Mountains since ~8 Ma (e.g., Cosentino et al., 2012; Meijers et al., 2018) and concomitant offshore subsidence (Walsh-Kennedy et al., 2014) developed the monoclinal flexure of Miocene rocks (Fernández-Blanco et al., 2019) as it divided the forearc basin into the landward uplifted Mut Basin, and the seaward subsided Cilicia Basin. Such coupled, short-wavelength vertical motions can be explained by the mechanism for thermo-viscous forearc high formation during the accretionary evolution of the south Anatolian margin along Central Cyprus (Fig. 5 & 12). The wavelength of uplift in the Central Taurus Mountains (Walsh-Kennedy *et al.*, 2014; Fernández-Blanco *et al.*, 2019) and the presence of the Cyprus slab under the range (e.g., Bakırcı *et al.*, 2012; Abgarmi *et al.*, 2017) agree well with thermo-viscous forearc models but

is inconsistent with models involving slab break-off (e.g., Schildgen *et al.*, 2014). The location of maximum uplift above the area of maximum thickness in the Anatolian crust (Fig. 3), the absence of accommodation structures along the uplifted area (Fernández-Blanco *et al.*, 2019) and the low seismicity along the margin (Imprescia *et al.*, 2012) are other observations compatible with broad upwarping due to deep crustal thickening beneath the modern Central Taurus Mountains.

The south Anatolian margin has a few unique characteristics that differentiate it from other accretionary margins worldwide. Arguably, foremost is the presence of the Troodos Ophiolite, emplaced within the forearc region. Its emplacement predates the tectonic events of this paper, but it could affect the mechanics of the wedge given its high strength relative to accreted sediments. Its position in the forearc is nevertheless primarily in the undeforming, "stable" section of the wedge, so it seems not to have affected tectonic processes trenchward or arcward.

Although every accretionary margin has its unique characteristics based on accretion history, volcanism, thermal conditions of the slab, and other variables, commonalities also exist. The thermo-viscous forearc high uplift presented here provides an explanation for the growth of broad, anomalously uplifted hinterland areas in other accretionary margins. These include the Kodiak and Eastern Aleutian islands, in the Alaskan margin; the Olympic Mts, in the Cascadia margin; the Nankai margin, and the Makran region, in southern Iran. These margins are mature and have arc-trench gaps of ~300 km, with large accretionary wedges and wedgetop basins, and forearc highs at >50 km of the trench-slope break. All these margins are also consistent with the principle characteristic of the viscous forearc model, a transient evolution, with a long history of sedimentation across a forearc, and the compartmentalization of deformation between basins and structural highs.

6. Conclusion

Our integration and interpretation of data in a transect along the Central Cyprus subduction suggest its evolution by subduction accretion since the Early Miocene. Simulations with 2D thermo-mechanical finite elements of accreting subduction wedges aimed at reproducing the first-order geology and vertical tectonic motions along the transect show that; (i) frictional-mechanical deformation driven by sediment accretion sets the time sequence of structures and the topo-bathymetry in the trench, trench slope and seaward areas of the forearc, and (ii) viscous-thermal deformation dominates in landward areas of the forearc and controls forearc high growth and its shape.

The resultant geometry of our models include closed wedge-top basins, including a large forearc basin that is later disrupted by the forearc high. Sedimentary filling of the wedge-top basins determines if, and how fast the accretionary wedge grows landward, and the growth by deformation of an initial, brittle forearc high above a curved slab, with no need for a mechanical backstop. Sedimentation in the forearc basin results in heating of the crust underneath, and if continued, a thermally-induced viscosity drop in the lower crust leads to weakening and ductile flow resulting in the uplift of a new forearc high, driven by ductile deformation. The occurrence, geometry, and timing of vertical motions along the accretionary margin and in the forearc high vary in relation to sediment availability, deposition rates and viscosity, through its dependence on temperature. While low sedimentation rates lead to thin forearc basins and results in forearc high uplifting at earlier times of margin accretion, progressively higher sedimentation rates result in more pronounced basin thickening, delaying surface uplift through brittle growth mechanisms. Similarly, lower viscosities produce prominent rounded-shaped forearc highs developing at earlier model run times, while increasing viscosities result in uplift of an area that develops at progressively younger times and has an increasingly flatter and broader top surface. Very

large sedimentation rates and/or higher viscosities stabilize the accretionary wedge and halt forearc high growth.

Models corroborate that ductile deformation, lead by thermally-activated viscosity at the base of the Anatolian crust and yielded by accretion of sediments incoming in the Cyprus Arc, is a viable mechanism driving the surface uplift that raised the modern Central Taurus Mountains. Our simulations reproduce upper plate deformation structures and modern sedimentary architectures along Central Cyprus and can be extrapolated to other accretionary margins with similar morphologies and vertical motions in time.

Acknowledgements

References

Abgarmi, B., Delph, J.R., Arda Ozacar, A., Beck, S.L., Zandt, G., Sandvol, E., Turkelli, N. & Berk Biryol, C. (2017) Structure of the crust and African slab beneath the central Anatolian plateau from receiver functions: New insights on isostatic compensation and slab dynamics. *Geosphere* 13, 1774–1787.

Aksu, A.E., Calon, T.J., Hall, J., Mansfield, S. & Yaşar, D. (2005) The Cilicia–Adana basin complex, Eastern Mediterranean: Neogene evolution of an active fore-arc basin in an obliquely convergent margin. *Marine Geology* 221, 121–159.

Bakırcı, T., Yoshizawa, K. & Özer, M. (2012) Three-dimensional S-wave structure of the upper mantle beneath Turkey from surface wave tomography. *Geophysical Journal International* 190, 1058–1076.

Biryol, C., Beck, S.L., Zandt, G. & Özacar, A. (2011) Segmented African lithosphere beneath the Anatolian region inferred from teleseismic P-wave tomography. *Geophysical Journal International* 184, 1037–1057.

Byrne, D.E., Wang, W.-H. & Davis, D.M. (1993) Mechanical role of backstops in the growth of forearcs. *Tectonics* 12, 123–144.

Calon, T.J., Aksu, A.E. & Hall, J. (2005a) The Neogene evolution of the Outer Latakia Basin and its extension into the Eastern Mesaoria Basin (Cyprus), Eastern Mediterranean. *Marine Geology* 221, 61–94.

Calon, T.J., Aksu, A.E. & Hall, J. (2005b) The Oligocene-Recent evolution of the Mesaoria Basin (Cyprus) and its western marine extension, Eastern Mediterranean. *Marine Geology* 221, 95–120.

Cassola, T. (2013) Mechanics of forearc basins. ETH Zurich

Christensen, N.I. & Mooney, W.D. (1995) Seismic velocity structure and composition of the continental crust: A global view. *Journal of geophysical research* 100, 9761–9788.

Çiner, A., Karabiyikoğlu, M., Monod, O., Deynoux, M. & Tuzcu, S. (2008) Late Cenozoic Sedimentary Evolution of the Antalya Basin, Southern Turkey. *Turkish Journal of Earth Sciences* 17, 1–41.

Cosentino, D., Schildgen, T., Cipollari, P., Faranda, C., Gliozzi, E., Hudáčková, N., Lucifora, S. & Strecker, M.R. (2012) Late Miocene surface uplift of the southern margin of the Central Anatolian Plateau, Central Taurides, Turkey. *GSA Bulletin* 124, 133–145.

Dahlen, F.A. (1984) Noncohesive critical Coulomb wedges: An exact solution. *Journal of Geophysical Research* 89, 10125–10133.

Davis, D., Suppe, J. & Dahlen, F.A. (1983) Mechanics of fold-and-thrust belts and accretionary wedges. *Journal of Geophysical Research*.

DeCelles, P.G. & Giles, K.A. (1996) Foreland basin systems. *Basin Research* 8, 105–123.

Delph, J.R., Abgarmi, B., Ward, K.M., Beck, S.L., Arda Özacar, A., Zandt, G., Sandvol, E., Türkelli, N. & Kalafat, D. (2017) The effects of subduction termination on the continental lithosphere: Linking volcanism, deformation, surface uplift, and slab tearing in central Anatolia. *Geosphere* 13, 1788–1805.

Dickinson, W.R. & Seely, D.R. (1979) Structure and stratigraphy of forearc regions. *AAPG Bulletin* 63, 2–31.

Dziewonski, A.M. & Anderson, D.L. (1981) Preliminary reference Earth model. *Physics of the Earth and Planetary Interiors* 25, 297–356.

Erdős, Z., Huismans, R.S. & van der Beek, P. (2015) First-order control of syntectonic sedimentation on crustal-scale structure of mountain belts. *Journal of Geophysical Research, [Solid Earth]* 120, 5362–5377.

Ergün, M., Okay, S., Sari, C., Zafer Oral, E., Ash, M., Hall, J. & Miller, H. (2005) Gravity anomalies of the Cyprus Arc and their tectonic implications. *Marine Geology* 221, 349–358.

Fernández-Blanco (2014) Evolution of Orogenic Plateaus at Subduction Zones: Sinking and raising the southern margin of the Central Anatolian Plateau. G. Bertotti (Ed). Ph.D. Vrije Universiteit Amsterdam

Fernández-Blanco, D., Bertotti, G., Aksu, A. & Hall, J. (2019) Monoclinal flexure of an orogenic plateau margin during subduction, south Turkey. *Basin Research* 13, 1774.

Fernández-Blanco, D., Bertotti, G., Aksu, A. & Hall, J. (2019) Monoclinal flexure of orogenic plateau margins during subduction, as recorded in south Turkey. *Basin Research* 31, :709–727.

Fernández-Blanco, D., Bertotti, G. & Çiner, A. (2013) Cenozoic tectonics of the Tuz Gölü Basin (Central Anatolia Plateau, Turkey). *Turkish Journal of Earth Sciences* 22, 715–738.

Fernández-Blanco, D., Mannu, U., Bertotti, G. & Willett, S.D. (2020) Forearc high uplift by lower crustal flow during growth of the Cyprus-Anatolian margin. *Earth and Planetary Science Letters* 544, 116314.

Fillon, C., Huismans, R.S. & van der Beek, P. (2013) Syntectonic sedimentation effects on the growth of fold-and-thrust belts. *Geology* 41, 83–86.

Flemings, P.B. & Saffer, D.M. (2018) Pressure and Stress Prediction in the Nankai Accretionary Prism: A Critical State Soil Mechanics Porosity-Based Approach. *Journal of Geophysical Research: Solid Earth* 123,

1089–1115.

Fuller, C.W. (2006) Controls on the Structural Morphology and Subduction-thrust Seismicity of Accretionary Margins. University of Washington

Fuller, C.W., Willett, S.D. & Brandon, M.T. (2006a) Formation of forearc basins and their influence on subduction zone earthquakes. *Geology* 34, 65–68.

Fuller, C.W., Willett, S.D., Fisher, D. & Lu, C.Y. (2006b) A thermomechanical wedge model of Taiwan constrained by fission-track thermochronometry. *Tectonophysics* 425, 1–24.

Fullsack, P. (1995) An arbitrary Lagrangian-Eulerian formulation for creeping flows and its application in tectonic models. *Geophysical Journal International* 120, 1–23.

Harrison, R.W., Newell, W.L., Batıhanlı, H., Panayides, I., McGeehin, J.P., Mahan, S.A., Őzhűr, A., Tsiolakis, E. & Necdet, M. (2004) Tectonic framework and Late Cenozoic tectonic history of the northern part of Cyprus: implications for earthquake hazards and regional tectonics. *Journal of Asian Earth Sciences* 23, 191–210.

Hofmeister, A.M. (1999) Mantle values of thermal conductivity and the geotherm from phonon lifetimes. *Science* 283, 1699–1706.

Ikari, M.J. & Kopf, A.J. (2011) Cohesive strength of clay-rich sediment. *Geophysical research letters* 38.

Imprescia, P., Pondrelli, S., Vannucci, G. & Gresta, S. (2012) Regional centroid moment tensor solutions in Cyprus from 1977 to the present and seismotectonic implications. *Journal of Seismology* 16, 147–167.

Jaupart, C. & Mareschal, J.C. (2005) Production from Heat Flow Data. *The Crust* 3, 65–84.

Koons, P.O. (1990) Two-sided orogen: Collision and erosion from the sandbox to the Southern Alps, New Zealand. *Geology* 18, 679–682.

Kopp, H. & Kukowski, N. (2003) Backstop geometry and accretionary mechanics of the Sunda margin. *Tectonics* 22.

Koulakov, I. & Sobolev, S.V. (2006) Moho depth and three-dimensional P and S structure of the crust and uppermost mantle in the Eastern Mediterranean and Middle East derived from tomographic inversion of local ISC data. *Geophysical Journal International* 164, 218–235.

Makris, J. & Stobbe, C. (1984) Physical properties and state of the crust and upper mantle of the Eastern Mediterranean Sea deduced from geophysical data. *Marine Geology* 55, 347–363.

McCay, G. (2010) Tectonic-sedimentary evolution of the Girne (Kyrenia) Range and the Mesarya (Mesaoria) Basin, North Cyprus. PhD. University of Edinburgh

McCay, G.A. & Robertson, A. (2013) Upper Miocene–Pleistocene deformation of the Girne (Kyrenia) Range and Dar Dere (Ovgos) lineaments, northern Cyprus: role in collision and tectonic escape in the …. *Geological Society, London*.

Meijers, M.J.M., Brocard, G.Y., Cosca, M.A., Lüdecke, T., Teyssier, C., Whitney, D.L. & Mulch, A. (2018) Rapid late Miocene surface uplift of the Central Anatolian Plateau margin. *Earth and Planetary Science Letters* 497, 29–41.

Mutlu, A. & Karabulut, H. (2011) Anisotropic Pn tomography of Turkey and adjacent regions. *Geophysical Journal International* 187, 1743–1758.

Nayar, K.G., Sharqawy, M.H., Banchik, L.D. & Lienhard, J.H., V. (2016) Thermophysical properties of seawater: A review and new correlations that include pressure dependence. *Desalination* 390, 1–24.

Özeren, M.S. & Holt, W.E. (2010) The dynamics of the eastern Mediterranean and eastern Turkey. *Geophysical Journal International* 183, 1165–1184.

Pasyanos, M.E. (2010) Lithospheric thickness modeled from long-period surface wave dispersion. *Tectonophysics* 481, 38–50.

Pavlis, T.L. & Bruhn, R.L. (1983) Deep-seated flow as a mechanism for the uplift of broad forearc ridges and its role in the exposure of high P/T metamorphic terranes. *Tectonics* 2, 473–497.

Platt, J.P. (1986) Dynamics of orogenic wedges and the uplift of high-pressure metamorphic rocks. *GSA Bulletin* 97, 1037–1053.

Pope, D.C. & Willett, S.D. (1998) Thermal-mechanical model for crustal thickening in the central Andes driven by ablative subduction. *Geology* 26, 511–514.

Ranalli, G. (1995) *Rheology of the Earth*. Springer Science & Business Media.

Reilinger, R., McClusky, S., Vernant, P., Lawrence, S., Ergintav, S., Cakmak, R., Ozener, H., Kadirov, F., Guliev, I., Stepanyan, R., Nadariya, M., Hahubia, G., Mahmoud, S., Sakr, K., ArRajehi, A., Paradissis, D., Al-Aydrus, A., Prilepin, M., Guseva, T., Evren, E., Dmitrotsa, A., Filikov, S.V., Gomez, F., Al-Ghazzi, R. & Karam, G. (2006) GPS constraints on continental deformation in the Africa-Arabia-Eurasia continental collision zone and implications for the dynamics of plate interactions: Eastern Mediterranean active tectonics. *Journal of Geophysical Research* 111.

Robertson, A.H.F. (1998a) Mesozoic-Tertiary tectonic evolution of the easternmost Mediterranean area: integration of marine and land evidence. *Proceedings of the Ocean Drilling Program. Scientific results Ocean Drilling Program*.

Robertson, A.H.F. (1998b) Tectonic significance of the Eratosthenes Seamount: a continental fragment in the process of collision with a subduction zone in the eastern Mediterranean (Ocean Drilling Program Leg 160). *Tectonophysics* 298, 63–82.

Schildgen, T.F., Yıldırım, C., Cosentino, D. & Strecker, M.R. (2014) Linking slab break-off, Hellenic trench retreat, and uplift of the Central and Eastern Anatolian plateaus. *Earth-Science Reviews* 128, 147–168.

Smit, J.H.W., Brun, J.P. & Sokoutis, D. (2003) Deformation of brittle-ductile thrust wedges in experiments and nature. *Journal of geophysical research* 108, 3.

Stephenson, R.A., Mart, Y., Okay, A., Robertson, A., Saintot, A., Stovba, S. & Khriachtchevskaia, O. (2004) TRANSMED Transect VIII: Eastern European Craton--Crimea--Black Sea--Anatolia--Cyprus--Levant Sea--Sinai--Red Sea. *The TRANSMED Atlas: The Mediterranean Region from Crust to Mantle*, 120–127.

Turcotte, D.L. & Schubert, G. (2002) *Geodynamics*. Cambridge.

Vanderhaeghe, O., Medvedev, S., Fullsack, P., Beaumont, C. & Jamieson, R.A. (2003) Evolution of orogenic wedges and continental plateaux: insights from crustal thermal–mechanical models overlying subducting mantle lithosphere. *Geophysical Journal International* 153, 27–51.

Walsh-Kennedy, S., Aksu, A.E., Hall, J., Hiscott, R.N., Yaltırak, C. & Çifçi, G. (2014) Source to sink: The development of the latest Messinian to Pliocene–Quaternary Cilicia and Adana Basins and their linkages with the onland Mut Basin, eastern Mediterranean. *Tectonophysics* 622, 1–21.

Willett, S.D. (1992) Dynamic and kinematic growth and change of a Coulomb wedge. In: K. R. McClay (Ed), *Thrust Tectonics*. Springer Netherlands, Dordrecht, pp. 19–31.

Willett, S.D. (1999) Orogeny and orography: The effects of erosion on the structure of mountain belts. *Journal of geophysical research* 104, 28957–28981.

Willett, S.D. & Schlunegger, F. (2010) The last phase of deposition in the Swiss Molasse Basin: from foredeep to negative-alpha basin. *Basin Research* 22, 623–639.

Figures & Tables

Figure 1. Accretionary margins in nature and models. Main morphotectonic features in **(A)** a generic accretionary margin with forearc high, in **(B)** models of subduction wedge accretion, and **(C)** their correlation to features in Central Cyprus. For natural examples, we use original definitions by Karig & Sharman (1975) and Dickinson & Seely (1979), and for numerical models a simpler nomenclature (e.g., Fuller, 1996). "Trench-fill basin" and "accretionary forearc basin" are the nature equivalents to "pro-wedge" and "wedge-top" basins in models, and the terms "residual" and "intramassif forearc basins" of Dickinson & Seely (1979) are in simulations the "landward" and "seaward" forearc basins, respectively. Correlation with elements along the Central Cyprus margin is based in Fernández-Blanco et al. (2020).

Figure 2. Model setup. Model setup, with specification of thermal and mechanical parameters. S is the point where the subducting plate contacts the Moho of the upper plate. A set of velocities, V, are defined with regards to a fixed frame in the upper-plate interior: Vx and Vy are the components of velocity in horizontal and vertical directions, respectively, and Vmech is the 2-D velocity in the mechanical domain and is a free variable. Boundary conditions are a constant convergence velocity, Vc, applied to the left side and the base of the subducting plate. Boundary between slab and upper plate has a frictional failure criterion, by which relative slip occurs on boundary once criterion is exceeded. The incoming sediments have a thickness of d_a. D_s is the flexural rigidity of the subducting plate and D_o is that of the overriding plate. The internal friction angle is shown as φ, and the friction angle between plates is φb. Aμ is the coefficient of the power-law viscosity and nμ is its coefficient, with Q being the activation energy. A = heat production, K = thermal conductivity, Cp = specific heat, C = cohesion and T = temperature. Material deforms viscously until yield stress is exceeded, at which point it deforms to satisfy yield criterion.

Figure 3. Transects along the Anatolian maring in Central Cyprus. Upper-crust and crustal-scale geological transects running N-S (650 km at around 33°30' E). The transects stretch from the Levantine Basin to the Tuz Gölü Basin across the Cyprus arc-trench, the island of Cyprus, the Cilicia Basin, the Central Taurus Mountains, and the Central Anatolian interior. The upper-left panel is a location map. Panel A is a transect across Central Cyprus and Anatolia, simplified from Stephenson et al. (2004), that has a topo-bathymetry with 3 times vertical exaggeration. EMed = East Mediterranean; CTM = Central Taurus Mountains; TGB = Tuz Golu Basin; CPM = Central Pontides Mountains; BkS = Black Sea. Panel B is the upper sector of the transect (up to 10 km depth), shown with vertical exaggeration of 7, and Panel C is the crustal cross-section for the area. These transects integrate upper crustal studies (Robertson, 1998; Stephenson et al., 2004; Calon et al., 2005a, 2005b; Çiner et al., 2008; McCay, 2010; Fernández-Blanco et al., 2013) with the interpretation of several geophysical studies (Ates et al., 1999; Mart & Ryan, 2002; Ergün et al., 2005; Koulakov & Sobolev, 2006; Özeren & Holt, 2010; Mutlu & Karabulut, 2011; Abgarmi et al., 2017; Delph et al., 2017), as detailed in Fernández-Blanco (2014). CVP = Central Volcanic Province.

Figure 4. Flow-law behavior of natural and simulated materials. Plot of effective viscosity vs temperature for natural and modeled materials under a constant strain rate (ϵ= 10^{-14}). Panel A shows the flow law behavior of olivine (+wet, +dry), in the upper right panel, as well as granite, quartz, plagioclase (An75) and quartzite (purple, blue, green and orange, respectively, in the main panel) alongside that of our Base Model material (black in both panels), and the ranges of parameter values in the viscous suites, which are shown in orange (for A_μ), in green (for n_μ) and in lilac (for Q) in the main panel. The table at the bottom shows the values and studies used. Panel B shows the flow law behavior of the models shown in Fig. 12; V1 (green); V2 (purple); V3 (orange); V4 (blue) and the Base Model material in black.

Figure 5. Base Model. Mechanical model evolution in time steps, with zoom-ins into the area where the forearc high develops. Times represented are, from top to bottom: 25Ma, 15Ma, 10Ma, 5Ma, and present. Strain rate is shown in vivid colors ranging from blue (low; -14.0 log_{10} s^{-1}) to red (high; -12.5 log_{10} s^{-1}). The mesh of black lines records cumulative deformation in the basement since model onset. The individual lines on top of the basement (white in main panels and black in zoom-in views) represent isochrones of deposited and subsequently deformed sediment.

Figure 6. Temperature, viscosity, and deformation during forearc high growth. Correlation among temperature (in °C, shown as black dashed lines), viscosity (in Pa·s, shown as gradient colors between blue -low- and yellow -high-), and the deformation mesh of the mechanical model (as a grid for the basement and originally-horizontal isochrones for the sedimentary cover, both in light white) in the area where the forearc high develops in 3 time steps: 25Ma, 10Ma, and present.

Figure 7. Variations in maximum sedimentation rates. Forearc high development with changes in maximum sedimentation rate. A) The figure shows models at 15 Ma, 5 Ma, and 0 Ma and includes an inset of the model where the forearc high develops, for the models with 0.1 mm/y (left column) and 0.9 mm/y (right column). The individual back lines on top of the basement represent isochrones that reflect deformation since their successive inception in time, and thus the overall geometric relationships expected for strata. A thicker black line marks the basement-infill contact. The dimmed grey box shows the approximate location of the zoom-in view. B) Line trace of the bottom of the crust and top of the basement in models with changes in sedimentation rates after a complete run. Vertical reference frame is taken

from the "S" point at the base of the crust. Upper panels are at 1:1 scale and the bottom panel is at 1:2 scale.

Figure 8. Variations in A_μ. Forearc high development with changes in the viscosity parameter Aμ. A) The figure shows 15 Ma, 5 Ma, and 0 Ma snapshots of an inset of the model where the forearc high develops, for the models with 6.46 x 10^{-6} MPa^{-n}/s (left column) and 13.09 x 10^{-6} MPa^{-n}/s (right column). The individual back lines on top of the basement represent isochrones that reflect deformation since their successive inception in time, and thus the overall geometric relationships expected for strata. A thicker black line marks the basement-infill contact. The dimmed grey box shows the approximate location of the zoom-in view. B) Line trace of the bottom of the crust and top of the basement in models with changes in the value of the viscosity parameter Aμ after a complete run. Vertical reference frame is taken from the "S" point at the base of the crust. Upper panels are at 1:1 scale and the bottom panel is at 1:2 scale.

Figure 9. Variations in n_μ. Forearc high development with changes in the stress exponent of viscosity, nμ. A) The figure shows 15 Ma, 5 Ma, and 0 Ma snapshots of an inset of the model where the forearc high develops, for the models with 2.45 (left column) and 2.85 (right column). The individual back lines on top of the basement represent isochrones that reflect deformation since their successive inception in time, and thus the overall geometric relationships expected for strata. A thicker black line marks the basement-infill contact. The dimmed grey box shows the approximate location of the zoom-in view. B) Line trace of the bottom of the crust and top of the basement in models with changes in the value of the viscosity parameter nμ after a complete run. Vertical reference frame is taken from the "S" point at the base of the crust. Upper panels are at 1:1 scale and the bottom panel is at 1:2 scale.

Figure 10. Variations in Q. Forearc high development with changes in the activation energy, Q. A) The figure shows 15 Ma, 5 Ma, and 0 Ma snapshots of an inset of the model where the forearc high develops, for the models with 150 kJ/mol (left column) and 190 kJ/mol (right column). The individual back lines on top of the basement represent isochrones that reflect deformation since their successive deposition in time, and thus the overall geometric relationships expected for strata. A thicker black line marks the basement-infill contact. The dimmed grey box shows the approximate location of the zoom-in view. B) Line trace of the bottom of the crust and top of the basement in models with changes in the value of the viscosity parameter Q after a complete run. Upper panels are at 1:1 scale and the bottom panel is at 1:2 scale.

Figure 11. Sedimentation rate and viscosity controls on wedge and basin morphology. Changes in wedge morphology and basin architecture as a function of maximum sedimentation rate and crustal viscosity shown along two axes that cross on the Base Model. The top-left to bottom-right diagonal shows models with varying sedimentation rates between 0 mm/yr in the top-left and 10 mm/yr in the bottom-right, with a fixed rheology model (Base Model -Fig. 4). The bottom-left to top-right diagonal shows models as a function of rheology, parameterized by effective log viscosity at 350°C and strain rate of 10-14 of 14.48 Pa·s in bottom-left to 16.38 Pa·s in the top-right. Effective viscosity models, V1 to V5, are shown in Fig. 4B. Light white lines show the deformation mesh of the mechanical model. A grid represents the basement and originally-horizontal lines are isochrones for the sedimentary cover, and their contact (top of the basement), is shown with thicker stroke. Isotherms are in dashed black lines, with numbers in °C. Figure shows the model sectors with morphological variations, between 150 km and 500 km, and excludes far sides, where wedge morphology is similar.

Figure 12. Conceptual evolution of the Anatolian margin in Central Cyprus.

Table 1. Main model parameters. Values of the main parameters used for the Base Model, their associated references and comments on the value choice. References in the table: (Dziewonski & Anderson, 1981; Christensen & Mooney, 1995); (Nayar *et al.*, 2016) (e.g., Davis *et al.*, 1983; Flemings & Saffer, 2018); (Ikari & Kopf, 2011); (Ranalli, 1995); (Fernández-Blanco *et al.*, 2020) (Reilinger *et al.*, 2006) (Makris & Stobbe, 1984) (Pasyanos, 2010) (Robertson, 1998a) (Hofmeister, 1999) (Jaupart & Mareschal, 2005) (Turcotte & Schubert, 2002)

Table 2. Models and parameterization. Models used in this study, the values of the four parameters that are changed systematically for the maximum sedimentation rate and viscosity suites, with reference to figures and videos of some representative simulations.

Supplementary material

Suppl. Material A. Model Design, formulation and routines.

The critical wedge theory explains how mechanical properties of accreting wedges control their geometry (Davis et al., 1983; Dahlen, 1984; Larroque et al., 1995; Malavieille, 2010), but excludes the ductile properties of these systems. Recent research inclusive of visco-plastic attributes show the influence of thermal or rheological variations or that of sediment load and/or competence in the strain distribution and deformation patterns within the accretionary wedge (e.g., Fuller et al., 2006; Willett and Schlunegger, 2010; Simpson, 2010; Fillon et al., 2013).

We used the coupled mechanical-thermal model of collisional wedges modified to account for features associated with a subduction wedge used in previous studies (Willett, 1992; Willett and Pope, 2004; Fuller et al., 2006). Our 2D kinematic-dynamic models consist of two coupled domains (Fig. 2). The domain where mechanical laws apply represents the crust of a deforming subduction zone. Accretion of incoming sediments is driven by the tangential velocities at the base of the mechanical domain. These velocities decrease toward, and become zero at, the "S" point, which represents the point of contact of the subducting slab and the continental Moho. The thermal domain covers the whole model, including the mechanical domain.

Boundary conditions

The simulation is governed by boundary conditions on velocity and frictional stick-slip along the domain limits. The plates converge by an horizontal velocity, v_c, which is set in the left

side of the model, while the right side is fixed in space. The "S" point, being the intersection point where the subducting slab meets the continental Moho, divides a left domain with a frictional stick-slip boundary condition, and a right domain with a zero tangential velocity boundary condition.

This set of boundary conditions allows the calculation of the slip in the interface between the subducting and overriding plates. This slip depends on the shear stress at the plate interface, τ, and the shear strength of the interface, τ_c, defined as:

$$\tau_c = \sigma_n \tan(\varphi_b), \tag{1}$$

where σ_n and φ_b are the normal force and friction angles at the plate interface, respectively. No slip at the interface occurs when $\tau < \tau_c$ and the overlying material is then "locked". Contrarily, if $\tau > \tau_c$ slip occurs. The amount of slip is found iteratively by applying $\tau = \tau_c$, i.e. the shear stress on the interface equals the shear strength. These boundary conditions entails the off-interface remaining at v_c to drive the deformation within the model.

Relevant subroutines

Flexural isostasy. Elastic deformation is excluded from the mechanical model and elastic plate flexure is explicitly included for the entire model. The plates respond isostatically to crustal loads by vertical motions, in which the deflection of the plate is calculated analytically. That is, the weight of the crust is applied as a load on both plates, which behave as semi-infinite, or broken, elastic plates (Hetényi and Hetbenyi, 1946) coupled at the "S" point to ensure their contact. Thus, the flexural rigidity of the plates and the density of the mantle, crust, and water layer, control the flexural response in both plates (Fuller, 1996).

Sedimentation. Models simulate deposition of continental sediments, which subsequently deform with properties similar to the rest of the crust. Models regard sediment source areas to be outside the domain of interest. This is, there is no internal mass balance and sediments represent an additional flux of mass into the forearc crust. Sediments fill depressions contained between structural highs to the limit of sediment availability. We use a maximum sedimentation rate to parametrize the availability of sediment. Sedimentation at the maximum rate fills basins while they are underfilled, and basins remain filled if subsidence is less than the maximum sedimentation rate. In the latter case, the resulting sedimentation rate is smaller than the maximum permissible sedimentation rate. In the models of this paper, the maximum sedimentation rate is the effective sedimentation rate throughout most of the main forearc basin except in its distal regions and smaller basins that may be overfilled and thus have a lower sedimentation rate. Models reproduce a synthetic stratigraphy by defining lines on the surface representing the tops of the horizontal sedimentary infill across specific time-intervals. These lines define isochronal surfaces that are subsequently tracked to understand deformation patterns since infill.

Thermal conditions. We equilibrate the thermal structure letting the thermal model run for 20 My before the onset of deformation. The temperature at the surface is 27 °C and the asthenospheric temperature at the model base is 1400 °C, and we use values for thermal conductivity of 2 and 50 W/(m·°K) for lithosphere and asthenosphere, respectively (Ranalli, 1995). Asthenospheric conductivity values are high to represent isothermal conditions. Heat production A = 0.85 μW/m3 (Jaupart & Mareschal, 2005) is included only in the crust and specific heat, Cp = 1200 J/Kg·°K is fixed for both model domains.

In the thermal domain, the temperature is computed using a finite element method that solves the advective-conductive heat transfer equation with radiogenic heat production:

$$\varrho c_p \frac{\alpha T}{\alpha t} = \frac{\alpha}{\alpha x}\left(k \ \frac{\alpha T}{\alpha x}\right) + \frac{\alpha}{\alpha z}\left(k \ \frac{\alpha T}{\alpha z}\right) - \varrho c_p \, v_x \frac{\alpha T}{\alpha z} - \varrho c_p \, v_z \frac{\alpha T}{\alpha z} + A, \tag{2}$$

in which ϱ is the density, c_p the specific heat, T the temperature, t the time, k the thermal conductivity, and v_x and v_z are the horizontal and vertical components of the velocity, respectively. The velocities in the remaining regions are assigned kinematically to ensure the conservation of heat and mass within the model domain. Heat production is included in a layer of thickness d_a, representing the region of the highest concentration of radiogenic elements in the crust. In the upper and lower surfaces, constant temperature boundary conditions are used, with the exception of the area where the subduction lithosphere reaches the base of the model. This area as well as the sides of the model have no heat flux. To simulate the thermal pre-collision situation in the subduction zone, the thermal model runs for a certain amount of time, t_{runup}, with a steady initial velocity field.

Suppl. Material B. Model Videos.

Videos the evolution of the mechanical model, with zoom-ins into the area where the forearc high develops. Videos represent. Strain rate is shown in vivid colors ranging from blue (low; -14.0 log_{10} s^{-1}) to red (high; -12.5 log_{10} s^{-1}). The gridded mesh of black lines records cumulative deformation in the basement since model onset. The individual white lines on

top of the basement represent isochrones of deposited and subsequently deformed material, a form of a synthetic stratigraphy. See Table 2 in the main text for information on the parameter values used. The videos are named:

- Vid_BaseModel - Base Model video
- Vid_n* - For videos varying the viscosity exponent, n_μ, where * = 2 for low values and * = 6 for high values (within the parameter spectrum checked, see Table 2).
- Vid_A* - For videos varying the viscosity pre-exponent, A_μ, where * = 2 for low values and * = 6 for high values (within the parameter spectrum checked, see Table 2).
- Vid_Q* - For videos varying the viscosity activation energy, Q, where * = 2 for low values and * = 6 for high values (within the parameter spectrum checked, see Table 2).
- Vid_Sr* - For videos varying sedimentation rate, with Sr0 = 0 mm/yr, Sr2 = 0.2 mm/y, Sr4 = 0.4 mm/y, Sr6 = 0.6 mm/y, Sr8 = 0.8 mm/y, Sr10 = 1.0 mm/y, Sr12 = 1.2 mm/yr (see Table 2).

References

Bakırcı, T., Yoshizawa, K., and Özer, M., 2012, Three-dimensional S-wave structure of the upper mantle beneath Turkey from surface wave tomography: Geophysical Journal International, v. 190, p. 1058–1076.

Biryol, C., Beck, S.L., Zandt, G., and Özacar, A., 2011, Segmented African lithosphere beneath the Anatolian region inferred from teleseismic P-wave tomography: Geophysical Journal International, v. 184, p. 1037–1057.

Calon, T.J., Aksu, A.E., and Hall, J., 2005a, The Neogene evolution of the Outer Latakia Basin and its extension into the Eastern Mesaoria Basin (Cyprus), Eastern Mediterranean: Marine Geology, v. 221, p. 61–94.

Calon, T.J., Aksu, A.E., and Hall, J., 2005b, The Oligocene-Recent evolution of the Mesaoria Basin (Cyprus) and its western marine extension, Eastern Mediterranean: Marine Geology, v. 221, p. 95–120.

Cassola, T. (2013). Mechanics of Forearc Basins. PhD thesis, Eidgenossiche Technische Hochschule (ETH).

Çiner, A., Karabiyikoğlu, M., Monod, O., Deynoux, M., and Tuzcu, S., 2008, Late Cenozoic Sedimentary Evolution of the Antalya Basin, Southern Turkey: Turkish Journal of Earth Sciences, v. 17.

Dahlen, F.A., 1984, Noncohesive critical Coulomb wedges: An exact solution: Journal of Geophysical Research, v. 89, p. 10125–10133.

Davis, D., Suppe, J., and Dahlen, F.A., 1983, Mechanics of fold-and-thrust belts and accretionary wedges: Journal of geophysical research, http://onlinelibrary.wiley.com/doi/10.1029/JB088iB02p01153/full.

Ergün, M., Okay, S., Sari, C., Zafer Oral, E., Ash, M., Hall, J., and Miller, H., 2005, Gravity anomalies of the Cyprus Arc and their tectonic implications: Marine Geology, v. 221, p. 349–358.

Fernández-Blanco, D. (2014) Evolution of Orogenic Plateaus at Subduction Zones: Sinking and raising the southern margin of the Central Anatolian Plateau.

Fernández-Blanco, D., Bertotti, G., Aksu, A. & Hall, J. (2019) Monoclinal flexure of an orogenic plateau margin during subduction, south Turkey. *Basin Research* 13, 1774.

Fernández-Blanco, D., Bertotti, G. & Çiner, A. (2013) Cenozoic tectonics of the Tuz Gölü Basin (Central Anatolia Plateau, Turkey). *Turkish Journal of Earth Sciences* 22, 715–738.

Fillon, C., Huismans, R.S., van der Beek, P., and Muñoz, J.A., 2013, Syntectonic sedimentation controls on the evolution of the southern Pyrenean fold-and-thrust belt: Inferences from coupled tectonic-surface processes models: Modeling of the Southern Pyrenean FTB: Journal of Geophysical Research: Solid Earth, v. 118, p. 5665–5680.

Forsyth, D.W., 1985, Subsurface loading and estimates of the flexural rigidity of continental lithosphere: Journal of Geophysical Research, v. 90, p. 12623.

Fuller, C.W. (1996). Controls on the Structural Morphology and Subduction Thrust Seismicity of Accretionary Margins. PhD thesis, University of Washington.

Fuller, C.W., Willett, S.D., and Brandon, M.T., 2006, Formation of forearc basins and their influence on subduction zone earthquakes: Geology, v. 34, p. 65–68.

Harrison, R.W., Newell, W.L., Batıhanlı, H., Panayides, I., McGeehin, J.P., Mahan, S.A., Őzhűr, A., Tsiolakis, E., and Necdet, M., 2004, Tectonic framework and Late Cenozoic tectonic history of the northern part of

Cyprus: implications for earthquake hazards and regional tectonics: Journal of Asian Earth Sciences, v. 23, p. 191–210.

Hetényi, M. and Hetbenyi, M. I. (1946). Beams on elastic foundation: theory with applications in the fields of civil and mechanical engineering, volume 16. University of Michigan Press.

Jaupart, C., and Mareschal, J.C., 2005, Production from Heat Flow Data: The crust, v. 3, p. 65–84.

Koulakov, I., and Sobolev, S.V., 2006, Moho depth and three-dimensional P and S structure of the crust and uppermost mantle in the Eastern Mediterranean and Middle East derived from tomographic inversion of local ISC data: Geophysical Journal International, v. 164, p. 218–235.

Larroque, C., Calassou, S., Malavieille, J., and Chanier, F., 1995, Experimental modelling of forearc basin development during accretionary wedge growth: Basin Research, v. 7, p. 255–268.

Luccio, F., and Pasyanos, M.E., 2007, Crustal and upper-mantle structure in the Eastern Mediterranean from the analysis of surface wave dispersion curves: Geophysical Journal International, v. 169, p. 1139–1152.

Makris, J., and Stobbe, C., 1984, Physical properties and state of the crust and upper mantle of the Eastern Mediterranean Sea deduced from geophysical data: Marine Geology, v. 55, p. 347–363.

Malavieille, J., 2010, Impact of erosion, sedimentation, and structural heritage on the structure and kinematics of orogenic wedges: Analog models and case studies: GSA Today, v. 20, p. 4–10.

McCay, G.A., Robertson, A.H.F., Kroon, D., Raffi, I., Ellam, R.M., and Necdet, M., 2013, Stratigraphy of Cretaceous to Lower Pliocene sediments in the northern part of Cyprus based on comparative 87 Sr/86 Sr isotopic, nannofossil and planktonic foraminiferal dating: Geological Magazine, v. 150, p. 333–359.

Mutlu, A.K., and Karabulut, H., 2011, Anisotropic Pn tomography of Turkey and adjacent regions: Geophysical Journal International, https://academic.oup.com/gji/article-abstract/187/3/1743/618417.

Özeren, M.S., and Holt, W.E., 2010, The dynamics of the eastern Mediterranean and eastern Turkey: Geophysical Journal International, v. 183, p. 1165–1184.

Reilinger, R., McClusky, S., Vernant, P., Lawrence, S., Ergintav, S., Cakmak, R., Ozener, H., Kadirov, F., Guliev, I., Stepanyan, R., Nadariya, M., Hahubia, G., Mahmoud, S., Sakr, K., et al., 2006, GPS constraints on continental deformation in the Africa-Arabia-Eurasia continental collision zone and implications for the dynamics of plate interactions: EASTERN MEDITERRANEAN ACTIVE TECTONICS: Journal of Geophysical Research, v. 111, doi: 10.1029/2005JB004051.

Robertson, A.H.F., 1998a, Mesozoic-Tertiary tectonic evolution of the easternmost Mediterranean area: integration of marine and land evidence: Proceedings of the Ocean Drilling Program, Scientific Results, Vol. 160; Chapter 54, http://www.era.lib.ed.ac.uk/handle/1842/559.

Robertson, A.H.F., 1998b, Tectonic significance of the Eratosthenes Seamount: a continental fragment in the process of collision with a subduction zone in the eastern Mediterranean (Ocean Drilling Program Leg 160): Tectonophysics, v. 298, p. 63–82.

Simpson, G.D.H., 2010, Formation of accretionary prisms influenced by sediment subduction and supplied by sediments from adjacent continents: Geology, v. 38, p. 131–134.

Stephenson, R.A., Mart, Y., Okay, A., Robertson, A., Saintot, A., Stovba, S., and Khriachtchevskaia, O., 2004, TRANSMED Transect VIII: Eastern European Craton--Crimea--Black Sea--Anatolia--Cyprus--Levant Sea--Sinai--Red Sea: The TRANSMED Atlas: The Mediterranean Region from Crust to Mantle, p. 120–127.

Willett, S.D., 1992, Dynamic and kinematic growth and change of a Coulomb wedge, *in* McClay, K.R. ed.,

Thrust Tectonics, Dordrecht, Springer Netherlands, p. 19–31.

Willett, S.D., and Pope, D.C., 2004, Thermo-mechanical models of convergent orogenesis: thermal and rheologic dependence of crustal deformation: Rheology and Deformation of the Lithosphere at Continental Margins. Columbia University Press, New York, NY, p. 179–222.

Willett, S.D., and Schlunegger, F., 2010, The last phase of deposition in the Swiss Molasse Basin: From foredeep to negative-alpha basin: Basin Research, v. 22, p. 623–639.